

A Unified Quasi-Spectral Viscosity (QSV) Approach to Shock Capturing and Large-Eddy Simulation

Victor C. B. Sousa^{a,*}, Carlo Scalo^{a,b}

^a*School of Mechanical Engineering, Purdue University, West Lafayette, IN, 47907*

^b*School of Aeronautics and Astronautics, Purdue University, West Lafayette, IN, 47907*

ARTICLE INFO

Article history:

Received 23 March 2021

Shock capturing,
Turbulence modeling,
Spectral Viscosity.

ABSTRACT

The Quasi-Spectral Viscosity (QSV) method is a novel closure for the filtered compressible Navier-Stokes equations. Its innovation lies on the introduction of a physical space implementation of a spectral-type viscosity by exploiting the residuals of filter transfer functions for both estimating the energy content near the grid cutoff and for modulating the dissipation magnitude at the different scales. Additionally, the proposed method is capable of unifying shock capturing and sub-filter scale modeling under a generalized Large-Eddy Simulation (LES) mathematical framework. The approach is tested extensively in one-dimensional shock-dominated problems, where it is shown to slightly outperform an artificial diffusivity based scheme. The QSV methodology is then extended to multi-dimensional test cases which gather both hydrodynamic turbulence and compressible flow phenomena. For example, QSV is able to simulate a Taylor Green Vortex with both sub and supersonic initial perturbations using identical structures. Satisfying results are also found for shock/vortex interactions, shock reflections off sinusoidal-walls and high speed turbulent channel flows, effectively achieving the unification of shock capturing and LES.

© 2023 Elsevier Inc. All rights reserved.

1. Introduction

Although hydrodynamic turbulence and shock formation have been treated separately in previous literature, both are phenomena characterized by an energy cascade from large to small scales due to nonlinear interactions (Frisch, 1995; Gupta and Scalo, 2018) and it is argued that they should be treated in a similar fashion. This unified approach with respect to energy distribution amongst scales on two fundamentally “distinct” phenomena can lead to achieving

*Corresponding author

e-mail: vsousa@purdue.edu (Victor C. B. Sousa)

accurate and numerically stable results of compressible high Reynolds number flows using relatively coarse grids even in the presence of shocks. An application that could benefit from such a development is the modeling hypersonic boundary layers due to steep, “shock-like”, flow gradients that can arise as a result of nonlinear dynamics in both transitional or fully turbulent regions.

The Large-Eddy Simulation (LES) methodology was developed to relax the Reynolds number constraint on numerical simulations of hydrodynamic turbulence. In a LES, the original Navier-Stokes equations are filtered via a low-pass band filtering operation which commutes with the spatial and temporal derivatives in an attempt to separate the large (filtered) scales from the small (sub filter) scales. Although such an operation is able to seamlessly separate the scales when applied to linear terms, when it acts upon nonlinear components, an unclosed term connected to energy flux between scales appears. The genesis of such a term is connected to the dynamics of large and small scales being coupled. Ultimately, the LES method directly computes the large scales evolution and models the energy flow towards the small scales via a dissipative term.

The effort spent in the development of subfilter-models for LES has been considerable and it was initially focused on incompressible flows. Most of these models are of the eddy-viscosity type, where the energy flux to small scales are modeled as being similar to the natural viscous dissipation process within a fluid. In such models, the fluid’s original kinematic viscosity field is augmented by an additional eddy-viscosity term ($\nu_t = \nu_c \ell$) whose magnitude is connected to a velocity scale near the filter’s cutoff (ν_c) and a mixing length (ℓ). These models have been defined both in the physical and spectral space.

The first model was proposed by Smagorinsky (1963a) who assumed that the small scale turbulent kinetic energy (TKE) production and dissipation are in equilibrium and that turbulence is in a state of statistical isotropy. One drawback of this model is that dissipation is always active: in regions of transitional flow or near boundaries, the model over predicts the dissipation leading to inaccurate results. This drawback was overcome by the introduction of the dynamic procedure (Germano et al., 1991; Lilly, 1992a). With this approach, the local dissipation was instantaneously modulated by accessing information near the grid cutoff by test filtering the resolved scales and averaging over homogeneous directions, as initially proposed, or, more locally, over Lagrangian fluid particle paths (Meneveau et al., 1996).

These models were extended to compressible Navier-Stokes equations. One example is Moin et al. (1991), who used the Favre filtered, continuity, momentum and internal energy equations to implement Germano’s dynamic procedure for compressible flows. He proposed models for the sub-filter stresses that arise in the momentum equations and for the sub-filter internal energy transport while opting to neglect the contribution of the pressure-dilation and turbulence dissipation rate terms. Moin et al. (1991) LES approach showed good agreement against experiments and DNS on setups with a turbulent Mach number up to $M_t = 0.4$. Moreover, as opposed to incompressible flows, where the trace of the subfilter stress tensor is absorbed in the pressure term, this approach modeled it separately, following Yoshizawa (1986)’s parametrization. Although this model was applied in simulations with no shocks, *a posteriori* results reported that the trace’s contribution could be as high as 50% as the its deviatoric counterpart.

These models, however, induce a flat wavenumber spectrum of dissipation, which is inconsistent with the studies

performed by Kraichnan (1976). He introduced the concept of a wavenumber-dependent eddy viscosity to model the energy transfer across a filter cutoff. This key result inspires the present work. If the cutoff lies in the inertial subrange, the resulting eddy viscosity dependence on wavenumber space exhibits a plateau at low wavenumbers and a cusp near the cutoff. Chollet and Lesieur (1981) reached similar conclusions by adopting the eddy-damped quasi-normal Markovian theory (EDQNM). Models that fail to enhance the dissipation rate near the cutoff wavenumber lead to a spurious accumulation of energy in the small scales, i.e. high wavenumber energy build up, as reported by Moin et al. (1991), for example.

Chollet and Lesieur (1981) proposed an exponential fit to the plateau-cusp behavior in the spectral space depending on a dimensional term comprising a velocity scale multiplied by a length scale. The information on such flow scales were extracted from the kinetic energy at the cutoff, $\sqrt{E(k_c)/k_c}$. This model, denoted spectral eddy viscosity (SEV), is also dynamic since at the early stages of the flow evolution, when there is still no energy at the cutoff, no dissipation is added in the system. Despite the solid theoretical foundations of this work, its applicability has been limited to homogeneous flows where the Navier-Stokes equations could be solved in spectral space. To expand this approach to inhomogeneous flows solved in the physical space, Metais and Lesieur (1992) introduced a constant wavenumber viscosity spectrum whose value was connected to the wavenumber-averaged “plateau-cusp” theoretical viscosity curve and estimated the energy at the cutoff via a structure function. Although very good agreement with DNS is reported, high wavenumber spectral energy build-up was observed.

The structure function model was also used in the context of compressible LES simulations (Normand and Lesieur, 1992; Ducros et al., 1995) where the sub-filter internal energy transport was modeled via a constant turbulent Prandtl number assumption. Other assumptions needed to extend the structure function model to a compressible flow involve considering coherent large structures to be sufficiently separated from the isotropic subgrid-scale (SGS) field and assumed to be not affected by compressibility. It was also mentioned that this would have no validity in the neighborhood of a shock although it could help in its numerical capturing. This model was used by Ducros et al. (1995) to simulate temporally developing supersonic boundary layers where the LES model was shown to stabilize the calculation once turbulence has been fully developed with only small effects on the dynamics of the unstable transition waves.

Although shocks in compressible flows arise from nonlinear wave steepening, entailing the generation of small scales just as in hydrodynamic turbulence, and although the same mathematical structure of filtered equations developed in LES could have been used to model such phenomena, they have been treated differently. Ducros et al. (1999) developed a shock capturing technique consisting of a sensor that triggers artificial dissipation in the shock region. The scheme was shown to thicken shocks so that they could be numerically resolved but the dissipation applied in the shock affected the turbulence that was interacting with it. Similar models of local artificial diffusivity were developed for shock turbulence interactions for example, in high-order structured simulations (Cook, 2007; Kawai and Lele, 2008; Kawai et al., 2010) and also in an unstructured spectral difference framework (Premasuthan et al., 2014a,b).

Concomitantly, a different method called Spectral Vanishing Viscosity (SVV) arose from the question of how to recover spectral convergence properties when dealing with conservation laws that exhibit spontaneous shock discon-

tinuities. Tadmor (1989, 1990) studied the use of Fourier-based discretization methods to solve the inviscid Burgers' equations and concluded that, if no regularization term was introduced, the numerical solution would not respect the unique entropy solution and convergence may fail. He then proposed to introduce a wavenumber-dependent viscosity term that would prevent oscillations and lead to convergence to the unique entropy solution. The idea was shown to be successful by mathematical proofs and numerical experiments. Subsequent work by Karamanos and Karniadakis (2000) and Pasquetti (2005) simply applied it to incompressible turbulent flows, via mere addition of the artificial SVV term to the momentum equation without further consideration. Moreover, Kirby and Karniadakis (2002) applied the same framework to compressible turbulent simulations and dissipation terms were added to the mass, momentum and energy equations. Although their results show that the method works, additional analysis on the reasons why it worked are lacking. In the same note, Pasquetti (2005) concludes his work stating that, although useful, the SVV-LES approach does not rely on physical arguments and therefore it only constitutes an efficient underlying platform above which a relevant sub-grid scale model should be added. The current manuscript addresses this important conceptual gaps in section 2.

In the current paper, a novel numerical scheme for conducting compressible flow simulations on coarse grids called Quasi-Spectral Viscosity (QSV) is presented. The scheme is based on solving the filtered Navier-Stokes equations using a common mathematical approach to model any type of sub-filter stresses, whether they are due to turbulence or shocks. In section 2, previous LES and artificial viscosity methods are presented and a parallel is drawn between them based on the analysis of the nonlinearities present in the Burgers' equation, functionally similar to those in incompressible LES; The performance of each method in this context is assessed and the Quasi-Spectral Viscosity (QSV) approach is first introduced. Following, section 3 discusses the fully detailed implementation of the QSV method focusing on how to estimate the magnitude of the fluctuations near the grid cutoff and on how to introduce a wavenumber modulation to the dissipation spectrum by using the residual of spatial filter operators. Next, in section 4, the compressible filtered Navier-Stokes equations are presented and the QSV-based closure models are proposed. Ultimately, section 5 gathers the performance of the QSV method, which is tested in 1D, 2D and three-dimensional setups ranging from shock dominated flows to quasi-incompressible turbulence. The test cases include the Sod shock tube problem, the Shu-Osher shock-entropy wave interaction, sub- and supersonic Taylor Green Vortex, shock/vortex interaction, shock reflection off a sinusoidal wall and compressible turbulent channel flow up to hypersonic bulk Mach numbers.

2. Reinterpretation and Assessment of Previous Eddy and Artificial Viscosity Methods

The objective of this section is to highlight similarities and establish a connection between different eddy viscosity models and the discontinuity regularization method based on artificial addition of a spectrally vanishing viscosity (SVV) (Tadmor, 1989, 1990). First, focus is given to hydrodynamic turbulence and its mathematical affinity to wave steepening and discontinuity formation. the normalized incompressible Navier-Stokes are taken under consideration:

$$\frac{\partial u_i}{\partial x_i} = 0, \quad (1)$$

$$\frac{\partial u_i}{\partial t} + \frac{\partial u_i u_j}{\partial x_j} = -\frac{\partial \mathcal{P}}{\partial x_i} + \frac{1}{Re} \frac{\partial^2 u_i}{\partial x_j \partial x_j}, \quad (2)$$

where $\mathcal{P} = p/\rho U^2$ and u_i are the nondimensionalized velocity components. These equations are then filtered by an operation that commutes with the derivation,

$$\bar{f}(\mathbf{x}) = \int f(\mathbf{x}') \bar{G}(\mathbf{x}, \mathbf{x}') d\mathbf{x}', \quad (3)$$

with an associated filter width ($\bar{\Delta}$) resulting in the filtered incompressible Navier Stokes:

$$\frac{\partial \bar{u}_i}{\partial x_i} = 0, \quad (4)$$

$$\frac{\partial \bar{u}_i}{\partial t} + \frac{\partial \bar{u}_i \bar{u}_j}{\partial x_j} = -\frac{\partial \bar{\mathcal{P}}}{\partial x_i} + \frac{1}{Re} \frac{\partial^2 \bar{u}_i}{\partial x_j \partial x_j} - \frac{\partial \tau_{ij}}{\partial x_j}, \quad (5)$$

where, $\tau_{ij} = \overline{u_i u_j} - \bar{u}_i \bar{u}_j$ is the subfilter scale (SFS) stress tensor, a remainder of the filtering operation applied to the nonlinear governing equations. Since the SFS term depends on the unresolved scales in the flow, it must be modeled. The modeling hypothesis is that the energy flux between the resolved scales and the subfilter scales can be parametrized as akin to a momentum diffusion process:

$$-\frac{\partial \tau_{ij}^d}{\partial x_j} = \frac{\partial}{\partial x_j} 2\nu_t \bar{S}_{ij}, \quad \tau_{ij}^d = \tau_{ij} - \frac{1}{3} \tau_{kk} \delta_{ij}, \quad \bar{S}_{ij} = \frac{1}{2} \left(\frac{\partial \bar{u}_i}{\partial x_j} + \frac{\partial \bar{u}_j}{\partial x_i} \right), \quad (6)$$

where the superscript ‘d’ indicates the deviatoric components and where ν_t is the eddy viscosity, previously discussed in section 1. In incompressible LES, the trace of the subfilter stress tensor (τ_{kk}) is absorbed into the pressure term. Now, if one uses the same framework to derive the filtered version of the inviscid Burgers’ equation, a prototypical representation of nonlinear scalar conservation laws that develops a discontinuity in a finite time, the result is:

$$\frac{\partial u_1}{\partial t} + \frac{1}{2} \frac{\partial u_1 u_1}{\partial x_1} = 0, \quad \frac{\partial \bar{u}_1}{\partial t} + \frac{1}{2} \frac{\partial \bar{u}_1 \bar{u}_1}{\partial x_1} = -\frac{1}{2} \frac{\partial \tau_{11}}{\partial x_1}. \quad (7)$$

Because of its simplicity, its parallel with the LES framework and its connection to solutions with discontinuities, the Burgers’ equation will be used as a test case for the Dynamic Smagorinsky (DYN), the Spectral Eddy Viscosity (SEV) and the SVV models. Previously, an overview of these models and their connection is provided hereafter.

2.1. Unified Mathematical Formulation for Eddy and Artificial Viscosity Methods

One starts by introducing the Germano et al. (1991)’s dynamic procedure, a way of instantaneously modulating the intensity (C) of the SFS model by comparing the energy content present in fields filtered with different strengths as an strategy to estimate the energy content of the smallest resolved scales. This resolves issues typically associated with the plain Smagorinsky model, which introduces excessive damping during flow transition and does not vanish at the boundaries in wall-bounded flows. In a simplified equation format it can be written as

$$\tau_{ij}^d = -2C\bar{\Delta}^2 |\bar{S}_{ij}| \bar{S}_{ij}. \quad (8)$$

Following, the Spectral Eddy Viscosity (SEV) model proposed by Chollet and Lesieur (1981) is presented. First, one starts with the sharp spectral filtered momentum equation in Fourier space,

$$\left[\frac{\partial}{\partial t} + (\nu + \nu_t(k, k_c))k^2 \right] \hat{u}(k, t) = t_{<k_c}(k, t), \quad (9)$$

for which the original model was developed. Here, the nonlinear triadic interaction among wavenumbers k , p and q such that $k, p, q < k_c$, i.e. nonlinear interaction between resolved scales is denoted with $t_{<k_c}(k, t)$ and the energy transfer to the subfilter scales is modeled via an eddy viscosity term (ν_t) that depends on the wavenumber (k) and its cutoff (k_c). Chollet and Lesieur (1981) analyzed the energy transfer assuming a Kolmogorov spectrum and modeled it as

$$\nu_t(k, k_c) = \nu_t^+(k/k_c) \sqrt{\frac{E(k_c)}{k_c}}, \quad \text{where} \quad \nu_t^+(k/k_c) = 0.267 + 9.21e^{-3.03k_c/k}, \quad (10)$$

which displays “plateau-cusp” behavior as a function of wavenumber. Moreover, analyzing the dimensionality of the term $\sqrt{E(k_c)/k_c}$, one concludes that it comprises the product of a length scale ($\ell = 1/k_c \approx 2\bar{\Delta}$) and a velocity scale ($v_c = \sqrt{k_c E(k_c)}$) related to the motion of the scales near the cutoff.

If one choses to represent the filtered momentum equation in Fourier space (9) in the physical domain, as in (5), an equivalent SFS stress tensor

$$-\tau_{ij}^d = \sqrt{\frac{E(k_c)}{k_c}} \left(\mathcal{F}^{-1}[\nu_t^+(k/k_c)] * \bar{S}_{ij} \right), \quad (11)$$

is reached where $*$ is the convolution operator and \mathcal{F}^{-1} is the inverse Fourier transform operation. The above relation also benefits from a change in perspective since it can be also rewritten as function of the residual of a low-band pass filter, i.e. a test filter (\tilde{G}), and as function of the local filter width $\bar{\Delta}$,

$$-\frac{\partial \tau_{ij}^d}{\partial x_j} = \frac{\partial}{\partial x_j} \left[\sqrt{2\bar{\Delta}E(k_c)} \left((1 - \tilde{G}) * \bar{S}_{ij} \right) \right]. \quad (12)$$

Note that, if the residual of a filtering operation can be used as a wavenumber modulation function for the eddy viscosity, one would able to implement such a model as a function of physical space operators. This is the core of the Quasi-Spectral Viscosity’s (QSV) approach will be further discussed in section 3. Furthermore, a connection is drawn between Germano et al. (1991)’s dynamic procedure and Chollet and Lesieur (1981) spectral eddy viscosity, since ultimately both models can be translated as using a filter stronger than the primary filter to inform the modeling of the unclosed terms.

Ultimately the Spectral Vanishing Viscosity (SVV) (Tadmor, 1989, 1990) method is addressed. It consists of adding an artificial dissipation term to the Burger’s equation with the objective to regularize its solutions and enable spectral convergence properties away from the discontinuity region. The method reads in equation format as,

$$\frac{\partial u}{\partial t} + \frac{1}{2} \frac{\partial uu}{\partial x} = \epsilon \frac{\partial}{\partial x} \left(Q * \frac{\partial u}{\partial x} \right), \quad (13)$$

where Q is a nonlinear viscosity kernel. Looking at such a formulation, one notes that it leads to a similar formulation to the filtered Burger's equation that arose from applying the LES mathematical framework (7). In conclusion, although previously unnoticed, the addition of the SVV term leads to the solution of the large scale field.

Moreover, Tadmor (1989, 1990) proved that the use of such a formulation leads spectral accuracy away from the discontinuity and stability if

$$\epsilon \geq \frac{1}{2k_c} \quad \text{and} \quad \hat{Q} \geq \text{Const} - \frac{1}{\epsilon k^2}. \quad (14)$$

From these, he interpreted that the minimum "artificial" dissipation needed to ensure spectral accuracy would need to be $\epsilon \approx \frac{1}{2k_c}$ and could be made to only act in modes above a certain activation wavenumber $m \sim k_c^\beta$, with $\beta < \frac{1}{2}$, rendering most of the spectrum inviscid. Here it should be pointed out that a formulation where Q affects all the scales, i.e. $m = 0$, is also consistent with the theoretical results, as pointed out by Karamanos and Karniadakis (2000) and that $1/2k_c$ is effectively an estimate for the length scale at the cutoff, as pointed out in the previous subsection.

Tadmor (1989, 1990)'s first proposed SVV implementation in a numerical experiment was

$$\hat{Q} = 1 - \hat{\tilde{G}} = \begin{cases} 0, & \text{if } |k| \leq m \\ 1, & \text{otherwise} \end{cases} \quad (15)$$

which, in the language of this work would be the residual of a sharp spectral test filter operation (\tilde{G}). His results, performed with $m = 2\sqrt{k_c}$, showed that the application of the regularization term made a previously unstable simulation converge. Moreover, it was noted that C^∞ smoothness of the viscosity's kernel wavenumber dependency improved the resolution of the method and it is speculated that looking for a smooth viscosity kernel made the numerical implementation closer to the exact SFS flux from large to small scales needed to hold a filtered solution.

In a subsequent work, Maday et al. (1993) analyzed the Burgers' equation in the context of a Legendre pseudo-spectral method and proved that the use of a SVV regularization term lead also to convergence to the exact entropy solution. In order to improve SVV's performance, Maday et al. (1993) proposed a viscosity kernel of the form

$$\hat{Q} = \begin{cases} e^{-(k-k_c)^2/(k-m)^2} & \text{if } |k| > m \\ 0, & \text{otherwise} \end{cases} \quad (16)$$

where $m = 5\sqrt{k_c}$ and $\epsilon = k_c^{-1}$. In this form, a vanishing viscosity magnitude which decreases continuously as the mode number decreases, is obtained.

In summary, a generalized format of sub-filter scale flux modeling consists of a magnitude pre-factor consisting of a length scale (ℓ) and velocity a velocity scale (v_c) near the filter's cutoff and a kernel (K) which is convolved with the strain rate tensor (S_{ij}), as in

$$\tau_{ij} = \ell v_c (K * S_{ij}). \quad (17)$$

Table 1 emphasizes the connection between the dynamic procedure (DYN), the SEV and the SVV methods and how they relate to the a generalized form (17). Moreover, table 1 foreshadows the QSV's methodology, based on

estimations of the energy content near the cutoff and on the dissipation modulation on wavenumber space via filter residuals, which will be dissected and analyzed in section 3.

	Length Scale (ℓ)	Velocity Scale (v_c)	Kernel (K)
DYN	$\bar{\Delta}$	$2C\bar{\Delta} \bar{S}_{ij} $	1
SEV	$1/k_c$	$\sqrt{k_c E(k_c)}$	$\mathcal{F}^{-1}[v_i^+(k/k_c)]$
SVV	ϵ	1	Q
QSV	$\bar{\Delta}$	$\sqrt{2E(k_c)/\bar{\Delta}}$	$1 - \tilde{G}$

Table 1: Summary of different eddy and artificial viscosity models and their connection to a generalized formulation.

2.2. Performance of DYN, SEV, SVV and QSV closures for Burgers' Equation

The Burgers' equation is solved in a periodic domain $x_1 \in [-1, 1]$, starting with with initial conditions

$$u_1(x, t = 0) = 1 + \frac{1}{2} \sin(\pi x), \quad (18)$$

until $t = 1$ using a pseudospectral Fourier method for the spatial derivatives and a 4th order Runge-Kutta scheme for the time integration. The results obtained using different eddy viscosity closures are then compared with the analytical solution based on the method of characteristics in the physical and spectral domain. In the current work, this procedure will be referred to as *a posteriori* analysis. In addition, an *a priori* analysis based on using the filtered analytical solution at time $t = 1$ as the input for each different model is also performed. The results in both physical and spectral space are gathered in figure 1.

It can be observed that the exact energy flux to subfilter scales spans across all resolved wavenumbers and it peaks near the cutoff (k_c). As discussed in the introduction (section 1), a wavenumber-dependent eddy viscosity with a plateau-cusp behavior was proposed to model the energy transfer across a filter cutoff in hydrodynamic turbulent flows (Kraichnan, 1976; Chollet and Lesieur, 1981). Figure 1, therefore, is an indication that a parallel can be drawn between the SEV model for hydrodynamic turbulence and accurate simulations of shock formation.

Now focus is given to the performance of the different models. First, it can be noted in figure 1 that the localization in physical space of the dynamic Smagorinsky procedure leads to a flat broadband response in the wavenumber space that overestimates dissipation at the large scales and underestimates it at scales near the filter's cutoff when modeling the SFS stress. The result of this spectral behavior when used to perform filtered simulations of inviscid Burgers' equation leads to spurious high-wavenumber build up due to the insufficient damping of the resolved scales near the cutoff. This is an undesirable behavior since it affects the overall accuracy of the solution in physical space, as observed by the presence of artificial high frequency oscillations.

Following, the *a priori* analysis of the SEV method shows that the growth of the magnitude of the modeled SFS stress components near the grid cutoff is able to follow more closely what is observed in the exact SFS stress although a certain degree of overdamping is introduced. In physical space, the dissipation's "cusp" behavior near the cutoff leads to τ_{11} being slightly non-local, following some of the oscillatory behavior of the analytical result. Moreover,

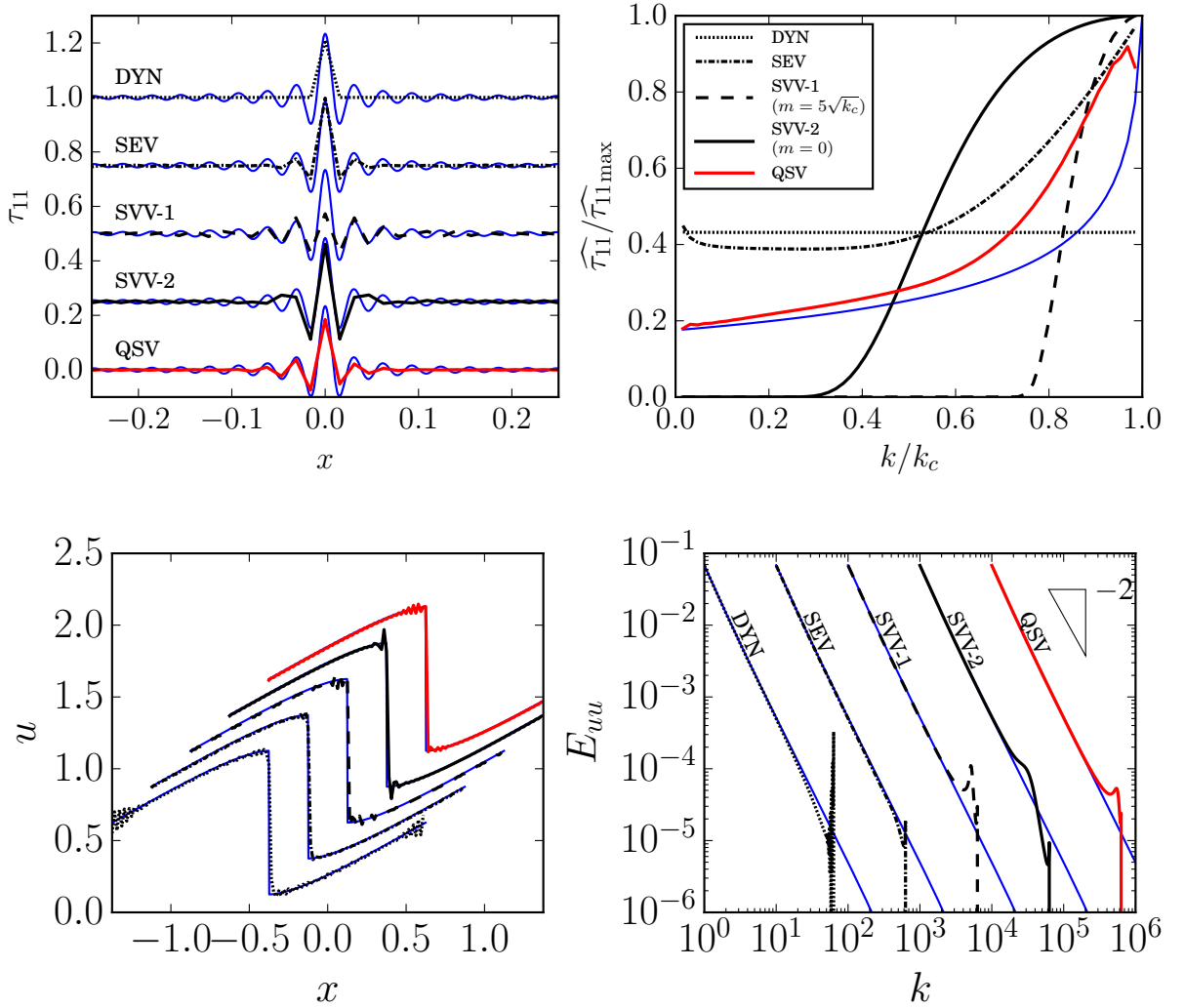


Fig. 1: Collection of both *a priori* (top) and *a posteriori* (bottom) analysis of the solution of the filtered Burgers' equation at time $t = 1$ with $N = 128$ grid points closed via different sub-filter models. Analytical results are shown in blue. Moreover, when needed, results are shifted for clarity.

the *a posteriori* results show that, in spite of some slight energy build up near the cutoff, the filtered solution follows the energy cascade of the exact solution closely. In the physical space, a mostly monotonic solution is achieved, with only low amplitude high frequency oscillations at the cutoff wavelength.

The SVV method is then analyzed by using both the suggested activation wavenumber $m = 5\sqrt{k_c}$ as well as $m = 0$. By studying the model in an *a priori* analysis, one can observe that the tentative of leaving part of the spectrum inviscid always leads to underdamping in the low wavenumber range. This reflects in the *a posteriori* solution as different degrees of energy accumulation near the cutoff in spectral space and overshoots in the physical space solution. Moreover, when a larger portion of the spectrum is left inviscid, the level of energy accumulation and amplitude of oscillations are higher. This effect is not limited to the solution of Burger's equation, as energy pile-up at high wavenumbers was also observed by Andreassen et al. (1994), while using the SVV method to perform

simulations of waves in a stratified atmosphere.

Despite not being the optimal way of introducing a spectral viscosity term, the SVV method does indeed lead to stable and accurate solutions as proved by Tadmor (1989). SVV paves a strong numerical theoretical background for the implementation of a spectral viscosity term in any hierarchical set of basis functions and its direct connection to the LES mathematical framework explicated in the current manuscript aims to widen its applications and strengthen its technical background when not applied to the initial setup where it was developed. Some examples of implementations of the standard SVV model using different methods are the Fourier (Tadmor, 1989, 1990), Legendre (Maday et al., 1993), Chebyshev Andreassen et al. (1994) and multi domain spectral methods, based on the spectral/hp Galerkin approach, by Karamanos and Karniadakis (2000).

Although the application of SEV models in different basis is an interesting topic, the current work chooses to focus on implementing such a model in physical space, in section 3, and its applications to both shock capturing and turbulence modeling. Nonetheless, a quick implementation of the current method in Legendre basis functions is introduced in Appendix A as a proof of concept.

Before presenting the inner workings of the QSV's method, though, its performance is compared against the previously discussed methods for eddy and artificial viscosity in figure 1. Keep in mind that these results are achieved by using the spatial operators developed in section 3: the Padé based method for estimating the energy at the cutoff and the effective test filter transfer function $\hat{G}_{\text{eff}}\left(\alpha, \beta, w, \frac{k}{k_c}\right)$. The values used for the filter strength, $\alpha = 0.45$, for the weighted average factor, $\beta = 0.8$, together with a 'DC' offset of $w = 0.85$ were used to generate the final curve. These parameters and their role in generating the ultimate transfer function is explained in the following section.

Figure 1 shows that the physical implementation with the described operators leads to a slight energy accumulation at the end of the resolved spectra, near the cutoff wavenumber. Despite the small pile-up, good agreement between the analytical and simulated results are recovered in both physical space and in the slope of the energy cascade in the low wavenumber range. When compared against the previous mentioned methods, it performs equally well or better in terms of the range of wavenumbers solved accurately. These results serve as a proof of concept that a spectral-like behavior can be introduced in physical space by the use of residuals of filtering operations.

3. Mathematical Formulation of the Quasi-Spectral Viscosity (QSV) Approach

In the current section the implementation of a spectrally modulated viscosity in physical domain, here denoted as the Quasi-Spectral Viscosity (QSV) approach, will be discussed. The two steps for implementing the method, first, estimating the cutoff energy, $E(k_c)$, in physical space, and second, introducing a "plateau-cusp" behavior as a function of wavenumber for the spectral viscosity only using spatial operators, are discussed in subsections 3.1 and 3.2.

Previously, an attempt to extend the SEV model to physical space was also addressed by Metais and Lesieur (1992), although it only focused on the cutoff energy estimation and not on the spectral modulation. Metais and Lesieur (1992) used a structure function to estimate $E(k_c)$ and averaged the viscosity kernel transfer function to be able to apply a constant coefficient in the wavenumber space. On top of not introducing the "plateau-cusp" behavior, the relation between $E(k_c)$ and the structure function is based on turbulence theory, which assumes local isotropy and

homogeneity at the small scales. In the current work, a different approach based on numerical operators, is proposed. Ultimately, the use of numerical theory should relax the assumptions needed to estimate the cutoff energy and also allow the introduction of a wavenumber modulation.

3.1. Cutoff Energy Estimation

The QSV method starts by analyzing the residual of a filter based on Padé operators (Lele, 1992). A family of sixth order implicit Padé filters is defined as

$$\alpha \tilde{f}_{i-1} + \tilde{f}_i + \alpha \tilde{f}_{i+1} = a_0 f_i + \sum_{j=1}^3 \frac{a_j}{2} (f_{i+j} + f_{i-j}), \quad (19)$$

where $\alpha \in (0, 0.5)$ is a parameter which controls the strength of the filter and its weights defined as a function of α are,

$$a_0 = \frac{11 + 10\alpha}{16}, \quad a_1 = \frac{15 + 34\alpha}{32}, \quad a_2 = \frac{-3 + 6\alpha}{16} \text{ and } a_3 = \frac{1 - 2\alpha}{32}. \quad (20)$$

From the filter's definition, one can arrive at its transfer function,

$$\hat{\tilde{G}}_{\text{Padé}} \left(\alpha, \frac{k}{k_c} \right) = \frac{a_0 + \sum_{j=1}^3 a_j \cos \left(j\pi \frac{k}{k_c} \right)}{1 + 2\alpha \cos \left(\pi \frac{k}{k_c} \right)}, \quad (21)$$

where $k_c = \pi/\Delta$.

Figure 2 shows that the residual of a Padé filter operation can serve as an estimate for the spectral energy content near the cutoff, i.e.

$$E(k_c) \approx 1 - \hat{\tilde{G}}_{\text{Padé}} \left(\alpha, \frac{k}{k_c} \right), \quad (22)$$

since it increases monotonically and can be made to concentrate near k_c even though a compact stencil is used. Nonetheless, the duality between frequency and physical spaces woven by the Fourier transform leads to the general principle that a function $f(x)$ and its Fourier transform $\hat{f}(k)$ can't be both highly localized. This principle is demonstrated in figure 2 by showing the physical residual of Padé filters with different α applied to a unitary step function located at $x = 0.5$. It can be observed that a higher α correlates not only with a concentration near the cutoff in the frequency space but also with a spreading motion in physical space. Ultimately, a trade-off must be found between the accuracy of the estimation of the spectral energy magnitude near the cutoff and the locality of the resulting operation.

In an attempt to improve the locality flexibility of the energy estimation operation, a scaling of the energy at cutoff term is proposed. First, it is considered that the most accurate $E(k_c)$ estimation for a certain grid discretization using the Padé filter's family is the one which the inflection point of the residual transfer function equals to 0.5 at the last resolvable mode prior to the cutoff. This previous statement is equivalent to saying that there exists a maximum α_{k_c} , which satisfies the following relation,

$$\hat{\tilde{G}}_{\text{Padé}} \left(\alpha_{k_c}, \frac{k_c - 1}{k_c} \right) = 0.5. \quad (23)$$

Moving forward, one can solve for the value of α_{k_c} and integrate the residual transfer function, $1 - \hat{G}_{\text{Pade}}\left(\alpha_{k_c}, \frac{k}{k_c}\right)$, to find a reference area connected to the best estimate for the amplitude of the energy at the cutoff for a certain grid size. In general, this integral is only a function of α , being

$$A(\alpha) = \int_0^1 \left(1 - \hat{G}_{\text{Pade}}\right) d(k/k_c) = \begin{cases} \frac{5}{16}, & \text{if } \alpha = 0, \\ \frac{\sqrt{1-4\alpha^2}-1+2\alpha\left[2\left(\sqrt{1-4\alpha^2}-1\right)+\alpha\left(14\alpha+2\sqrt{1-4\alpha^2}-1\right)\right]}{64\alpha^3}, & \text{if } 0 < \alpha < 0.5. \end{cases} \quad (24)$$

Now, if a more localized scheme for energy estimation is desired, one can scale the resulting residual operation by the area ratio between the maximum and desired α , reaching the results shown in figure 2. Ultimately, when applied to the 1D kinetic energy, the energy estimation operation is

$$E_{uu}(k_c) = \left[\left(1 - \hat{G}_{\text{Pade}}\right) * \frac{u^2}{2} \right] \frac{A(\alpha)}{A(\alpha_{k_c})}. \quad (25)$$

With this formulation, the information on the magnitude is preserved but the use of lower values of α lead to lower wavenumbers, or larger scales, being detected by sensor and again a trade-off must be sought. Although an optimal α might differ for each individual setup, the value of $\alpha = 0.45$ produces satisfying results for all the problems in the current manuscript.

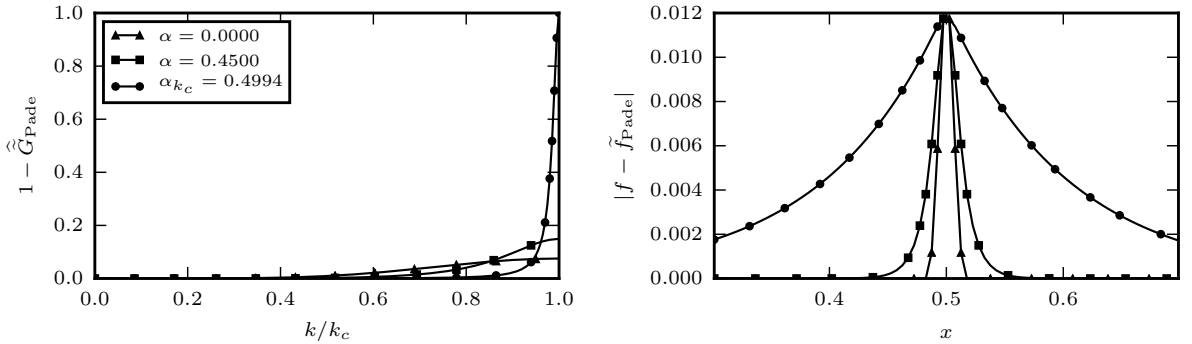


Fig. 2: Transfer functions obtained for truncated Fourier-Lagrange energy at the cutoff operator and the residual of a sixth order Padé filter when $k_c = 64$ (left) are shown together with the physical space result of a Padé residual operation when applied to a unitary step function located at $x = 0.5$ (right).

3.2. Wavenumber Modulation

The question of how to estimate the residual energy in physical space was addressed and now the problem of adding wavenumber dependency on the eddy viscosity term using only spatial operators will be tackled. For this, start by considering the Vandeven filter of order $p = 1$ (Vandeven, 1991),

$$\sigma_1(\eta) = 1 - \eta, \quad (26)$$

defined only on the resolved scales, i.e. $\eta \in [0, 1]$. A filter with such a transfer function was studied by Fejér (1903) in the context of looking for monotonic reconstructions of Fourier series partial sums and will be from now on referred

to as Fejér filter. Such a filter acts by modulating the amplitudes of the various Fourier components as

$$f^{\sigma_p} = \sum_{k=-k_c}^{k_c} \hat{f}_k \sigma_p(\eta) e^{ikx}, \quad (27)$$

where $\sigma_p = 1$ results in no filtering. Interestingly, the Fejér filter can be recovered as a spatial operator.

Starting from the spectral filter equation (27) applied to $u(x)$ and setting $k_c = M$, one substitutes \hat{u} for the discrete Fourier transform (DFT) operation,

$$u^{\sigma_1} = \sum_{k=-M}^M \left(\frac{1}{2Mc_k} \sum_{j=0}^{2M-1} u(x_j) e^{-ikx_j} \right) \left(1 - \frac{k}{M} \right) e^{ikx}, \quad (28)$$

where c_k is a term that appears due to aliasing on the last mode, being equal to 1 for $|k| < M$, and $c_k = 2$ for $k = \pm M$ (Shen et al., 2011). From this one can derive the operator that, when applied to the discrete values of the function, $u(x_j)$, where x_j are the collocation points $x_j = j \frac{2\pi}{2M}$, $0 \leq j \leq 2M - 1$, return its Fejér filtered value. From equation (28) one has that

$$u^{\sigma_1} = \sum_{j=0}^{2M-1} \left(\frac{1}{2M} \sum_{k=-M}^M \left(1 - \frac{k}{M} \right) \frac{1}{c_k} e^{ik(x-x_j)} \right) u(x_j) = \sum_{j=0}^{2M-1} H_j(x-x_j) u(x_j). \quad (29)$$

After some algebraic manipulation and using the help from the closed form of the Fejér kernel, the spatial Fejér filter operator is defined as

$$H_j(\theta) = \frac{\csc^2\left(\frac{\theta}{2}\right)}{2M(2M+2)} [1 - \cos(M\theta) + \sin(M\theta) \sin(\theta)] \quad (30)$$

where $\theta = x - x_j$. Ultimately, its implementation in a discrete grid where $x_j = j \frac{2\pi}{2M}$, $j = 0, 1, \dots, 2M - 1$ would be done by solving $u^{\sigma_1} = H_{ij} u_j$ where

$$H_{ij} = \begin{cases} \frac{4+2M}{2(2+2M)}, & \text{if } i = j \\ \frac{1}{2M(2+2M)} \csc^2\left(\frac{\pi(i-j)}{2M}\right) (1 - (-1)^{i-j}), & \text{otherwise.} \end{cases} \quad (31)$$

Ultimately, the arrived closed form is a global operator and if used in its complete form the same effect as performing the filter operation in spectral space would be returned. Casting it as a spatial operator, though, allows for the localization of the operation, a useful tool when modeling inhomogeneous flows.

To analyze how the truncation operation affects the Fejér filter operator note that, for a centered, explicit and symmetric scheme, generically represented here as,

$$\tilde{G}_i = a_0 G_i + \sum_{j=1}^{n_w} \frac{a_j}{2} (G_{i+j} + G_{i-j}), \quad (32)$$

its transfer function can be represented as

$$\hat{\tilde{G}}\left(\frac{k}{k_c}\right) = a_0 + \sum_{j=1}^{n_w} a_j \cos\left(j\pi \frac{k}{k_c}\right), \quad (33)$$

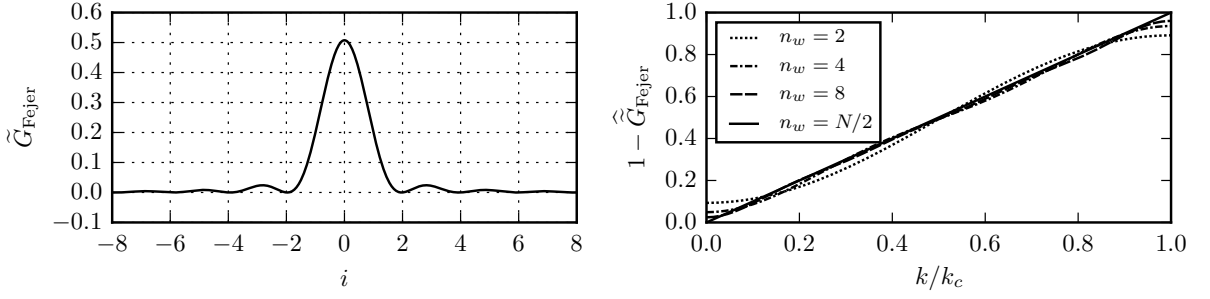


Fig. 3: The Fejér kernel in space and its self windowed behavior is shown on the left for $N = 128$. On the right, the related transfer function obtained for the global ($n_w = N/2$) and for the truncated operators for different window widths n_w .

where $k_c = \pi/\Delta$. Figure 3 shows that the self windowed nature of the weights of the Fejér filter spatial operator makes its transfer function converge quickly to the theoretical straight line independently of the number of the total number of modes. This behavior renders the truncated version of the operator useful.

Following, an linear combination between the residuals of the truncated spatial Fejér filter operator and the previously mentioned Padé filter is used with the objective to decrease the over dissipation introduced by the modeled SFS flux in the middle range of wavenumbers when only the Fejér filter were used. Additionally, if only a Padé filter were used a similar overdissipation problem would have happened but now at the low wavenumber range. The linear combination, ultimately, allows for tailoring the wavenumber response of modeled SFS flux to be closer to the “plateau-cusp” behavior observed in the *a priori* analysis (see figure 1) by using an following effective test filter

$$\hat{\hat{G}}_{\text{eff}} \left(\alpha, \beta, w, \frac{k}{k_c} \right) = w \left[1 - \beta \hat{\hat{G}}_{\text{Pade}} \left(\alpha, \frac{k}{k_c} \right) + (1 - \beta) \hat{\hat{G}}_{\text{Fejer}} \left(\frac{k}{k_c} \right) \right]. \quad (34)$$

4. Application of the Quasi-Spectral Viscosity Closure in the Filtered Compressible Navier-Stokes Equations

In this section, the compressible implementation of Large Scale Simulations (LSS) focusing on the unification of the treatment between shocks and turbulent eddies will be discussed. First the governing equations will be derived from the compressible Navier-Stokes relations using filtering operations and the unclosed terms as well as their closure will be presented.

4.1. Governing Equations

The compressible Navier-Stokes system of equations can also be filtered by an operation that commutes with the derivation, as described by (3), similarly to its incompressible counterpart (5). After the initial filtering, two routes could be chosen, the Reynolds-based or the Favre-based filtered equations. By using the Reynolds method, all equations in the system would require closure models and the role of small-scale density variations would have to be modeled specifically. Sidharth and Candler (2018) argued that modeling the SFS flux in the density field separately could lead to an improvement in LES of variable-density turbulence. On the other hand, the use of the Favre-based

method leads to implicitly solving density related nonlinear terms by defining the Favre filter operation as,

$$\check{f} = \frac{\overline{\rho f}}{\bar{\rho}}. \quad (35)$$

In the end, solving for the Favre filtered quantities (\check{f}) simplifies the LES equations for compressible flows. Moreover, compressible LES implementations based on the Favre-filtered equations were already successfully performed with different closure models by, for example, Moin et al. (1991), Normand and Lesieur (1992), Vreman et al. (1995) and Nagarajan et al. (2003). In this work, we follow the path of the latter, and derive the Favre-filtered Navier-Stokes relations introducing a pressure correction based on the sub-grid contribution to the velocity advection,

$$\frac{\partial \bar{p}}{\partial t} + \frac{\partial \bar{\rho} \check{u}_j}{\partial x_j} = 0, \quad (36)$$

$$\frac{\partial \bar{\rho} \check{u}_i}{\partial t} + \frac{\partial \bar{\rho} \check{u}_i \check{u}_j}{\partial x_j} = -\frac{\partial \bar{p}}{\partial x_i} + \frac{\partial \mu \check{\sigma}_{ij}}{\partial x_j} - \frac{\partial \bar{\rho} \tau_{ij}}{\partial x_j}, \quad (37)$$

$$\frac{\partial \bar{E}}{\partial t} + \frac{\partial (\bar{E} + \bar{p}) \check{u}_j}{\partial x_j} = \frac{\partial}{\partial x_j} \left(k \frac{\partial \check{T}}{\partial x_j} \right) + \frac{\partial \mu \check{\sigma}_{ij} \check{u}_i}{\partial x_j} - \frac{\partial \bar{\rho} C_p q_j}{\partial x_j} - \frac{\partial}{\partial x_j} \left(\frac{1}{2} \bar{\rho} \pi_j \right) + \mu \epsilon, \quad (38)$$

$$\frac{\bar{p}}{\gamma - 1} = \bar{E} - \frac{1}{2} \bar{\rho} \check{u}_i \check{u}_i - \frac{1}{2} \bar{\rho} \tau_{ii}. \quad (39)$$

The nonlinear terms that contribute to the energy flux from large to small scales are, the SFS stress tensor,

$$\tau_{ij} = \widetilde{u_i u_j} - \check{u}_i \check{u}_j, \quad (40)$$

the SFS temperature flux,

$$q_j = \widetilde{T u_j} - \check{T} \check{u}_j, \quad (41)$$

the SFS kinetic energy advection,

$$\pi_j = \widetilde{u_k u_k u_j} - \check{u}_k \check{u}_k \check{u}_j \quad (42)$$

and the SFS turbulent heat dissipation

$$\epsilon = \frac{\partial \overline{\sigma_{ij} u_i}}{\partial x_j} - \frac{\partial \check{\sigma}_{ij} \check{u}_i}{\partial x_j}. \quad (43)$$

Subfilter contributions resulting from the nonlinearities involving either the molecular viscosity or conductivity's dependency on temperature have been neglected following Vreman et al. (1995), who showed those are negligible in comparison against the other terms' magnitudes. Following Nagarajan et al. (2003), π_j and ϵ are neglected.

4.2. QSV's Navier-Stokes Closure

A complete model for performing compressible large scale simulations that could include both shocks and turbulent events is proposed as,

$$\tau_{ij} = -C_{\tau_{ij}} \frac{1}{2} \left(\frac{\partial \ddot{u}_i}{\partial x_j} + \frac{\partial \ddot{u}_j}{\partial x_i} \right), \quad (44)$$

$$q_j = -C_q \frac{\partial \ddot{T}}{\partial x_j}, \quad (45)$$

where the double dot superscript indicates the filter modulated quantities, defined as

$$\frac{\partial \ddot{u}_i}{\partial x_j} = \sqrt{2 \|\bar{\Delta}_l E_{u_j u_j}(k_{c,l})\|} \left[\frac{\partial \check{u}_i}{\partial x_j} * \left(1 - \tilde{G}_{\text{eff}}(\alpha, \beta, w) \right) \right], \quad (46)$$

$$\frac{\partial \ddot{T}}{\partial x_j} = \sqrt{2 \|\bar{\Delta}_l E_{u_j u_j}(k_{c,l})\|} \left[\frac{\partial \check{T}}{\partial x_j} * \left(1 - \tilde{G}_{\text{eff}}(\alpha, \beta, w) \right) \right], \quad (47)$$

$\|\cdot\|$ is the 2-norm operator for the vector components $l = 1, 2$ and 3 . It is possible that the cutoff energy estimation procedure will lead to large variations in space when highly localized flow features, such as shocks, do not align with the grid or the grid itself is deformed. In those cases, smoothing procedure, i.e. a gaussian filter (Cook, 2007), can be performed after taking the squared root.

The canonical test case of 1D Riemann shock tube problem (Sod, 1978) was used to inform the magnitude of the constant factor in front of the sub-filter scale temperature flux, which was set to $C_q = 0.6$. A complete account of the simulations and results can be found in Appendix B. Moreover, an *a priori* of the Taylor Green Vortex (TGV) (section 5.2) revealed that the magnitude coefficient ($C_{\tau_{ij}}$) needed to be lower if off-diagonal terms were being considered. This lead to setting

$$C_{\tau_{ij}} = \begin{cases} 1.0, & \text{if } i = j \\ 0.6, & \text{if } i \neq j. \end{cases} \quad (48)$$

The need of decreasing the magnitude for SFS heat flux and for the off-diagonal of the SFS stress tensor could be related to a nonlinear coupling strength that decreases when the nonlinear term is not comprised of a field acting on itself. Although this justification seems straightforward, further analysis to support this statement is needed.

The coefficients α, β and w were gathered from *a priori* analysis of the Burgers' equation (section 2.2), of the 1D Riemann shock tube problem (Sod, 1978) (Appendix B). It was found that $\alpha = 0.45$ and $\beta = 0.8$ led to satisfactory transfer function shapes for both τ_{ij} and q_j . The weight factor w used to introduce a 'DC' offset in the transfer functions differed for τ_{ij} and q_j being 0.85 and 0.95, respectively.

Historically, the treatment of the subfilter stress tensor τ_{ij} was done by separating its deviatoric and isotropic components. Models for the deviatoric part were then extended from incompressible models and the trace of τ_{ij} was either modeled differently (Moin et al., 1991) or neglected (Ng and Erlebacher, 1992; Normand and Lesieur, 1992; Ducros et al., 1995). Throughout this manuscript, though, a model based on incompressible turbulence closures was successfully extended to simulated discontinuities and it is hypothesized that modeling τ_{ij} based on \check{S}_{ij} (44) instead of its trace free counterpart will lead to a unification of shock capturing and turbulence modeling.

5. Performance Assessment of the QSV's closure

In this section, the proposed QSV's closure will be tested and compared against previous LES and shock capturing models in setups that range from shock-dominated flows to quasi-incompressible turbulence. First, the 1D Riemann shock tube problem (Sod, 1978) and the Shu-Osher shock-entropy wave interaction (Shu and Osher, 1988) problems are tackled. Following, a compressible Taylor-Green vortex setup ranging from sub to supersonic initial conditions is simulated and analyzed. Further test cases are proposed to test and establish the QSV method, such as a shock-wave vortex interaction, a shock-sinusoidal wall reflection and a turbulent channel flow up to hypersonic turbulent bulk Mach numbers. The aforementioned test cases are solved using a 6th-order Padé compact finite difference scheme (Lele, 1992) coupled with a 3rd-order Runge-Kutta time integration method.

5.1. One-dimensional Shock Dominated Flows

The Favre-filtered one-dimensional compressible Euler equations read,

$$\frac{\partial \bar{\rho}}{\partial t} + \frac{\partial \bar{\rho} \tilde{u}_1}{\partial x_1} = 0, \quad (49)$$

$$\frac{\partial \bar{\rho} \tilde{u}_1}{\partial t} + \frac{\partial \bar{\rho} \tilde{u}_1 \tilde{u}_1}{\partial x_1} = -\frac{\partial \bar{p}}{\partial x_1} - \frac{\partial \bar{\rho} \tau_{11}}{\partial x_1}, \quad (50)$$

$$\frac{\partial \bar{E}}{\partial t} + \frac{\partial (\bar{E} + \bar{p}) \tilde{u}_1}{\partial x_1} = -\frac{\partial}{\partial x_1} (\bar{\rho} C_p q_1), \quad (51)$$

$$\frac{\bar{p}}{\gamma - 1} = \bar{E} - \frac{1}{2} \bar{\rho} \tilde{u}_1 \tilde{u}_1 - \frac{1}{2} \bar{\rho} \tau_{11}, \quad (52)$$

where the viscous and conductive effects are neglected and where τ_{11} and q_1 are the sub-filter flux terms. If this system of equations is initialized the following initial conditions in density, velocity and pressure,

$$[\rho, u, p](x, 0) = \begin{cases} [1, 0, 1], & \text{if } x < 0.0 \\ [0.125, 0, 0.1], & \text{otherwise,} \end{cases} \quad (53)$$

then, a single shockwave propagating to the right develops and can be sustained by a Dirichlet supersonic inflow boundary condition on the left and an Neumann outflow boundary condition on the right. As the flow evolves, its exact solution leads to 4 constant density states separated by a shock, a contact discontinuity and a rarefaction wave, as shown in figure 4 at time $t = 0.2$. Shocks and rarefaction regions are also seen in the pressure and velocity fields.

The results for this test case, known as the Sod shock tube problem (Sod, 1978), obtained via the QSV model are then compared against the Local Artificial Diffusivity (LAD) model (Cook, 2007; Kawai and Lele, 2008; Kawai et al., 2010). Figure 4 gathers a grid sensitivity study of the models considered. The QSV model is shown both with and without the application of an explicit filter, in dotted black and solid red, respectively. The explicit filtering step, here performed by a Padé filter (21) with $\alpha = 0.499$, is able to attenuate spurious high wavenumber oscillations that are present in the results, especially on coarse grids.

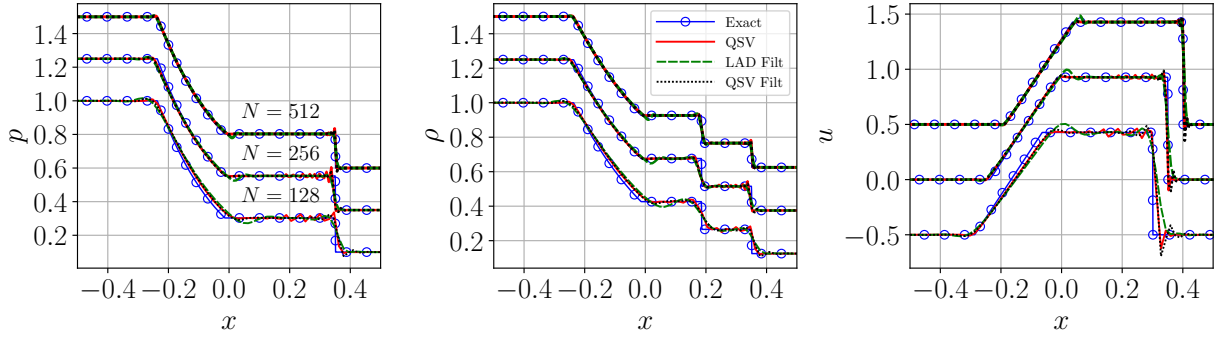


Fig. 4: Sod shock tube results at $t = 0.2$ computed using the Local Artificial Diffusivity (LAD) method, which requires explicit filtering, and the Quasi-Spectral Viscosity (QSV) method with and without the explicit filtering operation, are compared with the analytical solution.

Different behaviors of the QSV and the LAD approaches are observed in the velocity field. Although both models appropriately capture the shock, the LAD method leads to an overshoot near the center of the domain at the foot of the expansion wave, whereas the QSV retains a higher degree of monotonicity at the same location. In the shock region though, the LAD model smoothly reaches the right quiescent state, whereas the QSV exhibits an undershoot. The LAD implementation requires a Padé explicit filtering step (Kawai et al., 2010) with $\alpha = 0.495$, probably due to difficulties with energy build up at high wavenumbers. In contrast, this step is not required in the QSV method, although, if used, a lower degree of filtering, i.e. a higher value of α , is already sufficient to control high wavenumber oscillations.

Moving forward, another one dimensional canonical problem, the shock-entropy wave interaction introduced by Shu and Osher (1988), is tackled. The setup comprises a shock wave propagating into a sinusoidally perturbed resting fluid which, upon interaction, are compressed and acoustic waves are generated. The generated waves have sufficient magnitude to induce wave steepening by themselves and ultimately generate a train of weak shocks downstream of the primary shock. This problem is defined by the following initial conditions in the domain $x \in [-1, 1]$,

$$[\rho, u, p](x, 0) = \begin{cases} [3.857143, 2.629369, 10.333333], & \text{if } x < -0.8 \\ [1.0 + 0.2 \sin(5\pi x), 0.0, 1.0], & \text{otherwise.} \end{cases} \quad (54)$$

The initial conditions are advanced up until $t = 0.36$ using a timestep of $\delta t = 1 \times 10^{-5}$ and results are gathered in figure 5.

Once more, results are shown for the QSV model with and without the explicit filtering step and for the LAD model using the same color scheme as in figure 4. The three approaches converge to the qualitatively similar results as the grid is refined. One key aspect to be observed in the simulation of a Shu-Osher problem (Shu and Osher, 1988) is how much dissipation is introduced in the trailing-shock density oscillations by a shock-capturing method. In this aspect, the QSV method outperforms the LAD scheme, being able to retain the magnitude of such density oscillations even at coarse grids. The introduction of a smaller dissipation levels by the QSV technique, though, leads to higher levels of spurious pressure oscillations and velocity undershoots. These do not represent a problem, though, since they are easily controlled by the explicit filtering step using the Padé filter with $\alpha = 0.499$.

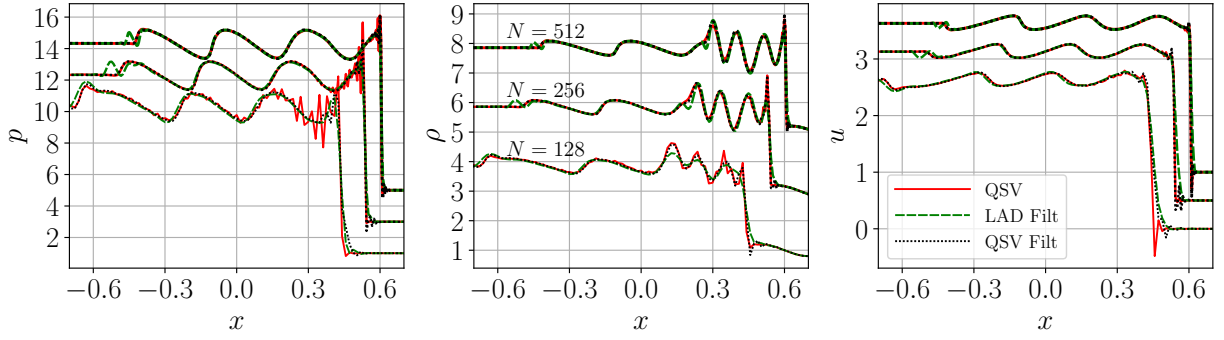


Fig. 5: Shu-Osher shock entropy wave interaction results at $t = 0.36$ computed using the Local Artificial Diffusivity (LAD) method, which requires explicit filtering, and the Quasi-Spectral Viscosity (QSV) method with and without the explicit filtering operation, are compared with the analytical solution

In a previous attempt, Maday et al. (1993) used the Spectrally Vanishing Viscosity (SVV) methodology to stabilize Sod shock tube and Shu-Osher shock-entropy wave interaction simulations using a Legendre based discretization. The SVV kernel (16) was simply extended to the continuity, momentum and energy equations without further considerations. Their results using 128 modes to resolve the Sod shock tube and 220 modes for the Shu-Osher problem display higher amplitude spurious oscillations in both density and velocity fields when compared to the current results. The oscillations in the pressure field, though, are of similar magnitude in comparison when no filtering is applied. Moreover, QSV was also implemented using a Legendre-Galerkin discretization as a proof of concept and its results for solving the Sod and Shu-Osher test cases are gathered in Appendix A.

5.2. Taylor Green Vortex (TGV)

The complete QSV closure relations (44) - (45) are now tested by assessing their capability of modeling the energy flux from large to small scales 3D turbulence problems, specifically via *a priori* and *a posteriori* analysis of the evolution of the Taylor-Green vortex (TGV), where the initial large-scale vortices breakdown and generate an energy cascade that feeds small-scale turbulence. The TGV is defined at $t = 0$ in a cubic domain $\Omega \in [-\pi L, \pi L]^3$ as,

$$\rho(\mathbf{x}, 0)/\rho_0 = 1, \quad (55)$$

$$u_1(\mathbf{x}, 0)/V_0 = \sin\left(\frac{x_1}{L}\right) \cos\left(\frac{x_2}{L}\right) \cos\left(\frac{x_3}{L}\right), \quad (56)$$

$$u_2(\mathbf{x}, 0)/V_0 = -\cos\left(\frac{x_1}{L}\right) \sin\left(\frac{x_2}{L}\right) \cos\left(\frac{x_3}{L}\right), \quad (57)$$

$$u_3(\mathbf{x}, 0)/V_0 = 0, \quad (58)$$

$$p(\mathbf{x}, 0)/\rho_0 V_0^2 = \frac{p_0}{\rho_0 V_0^2} + \frac{1}{16} \left[\cos\left(\frac{2x_1}{L}\right) + \cos\left(\frac{2x_2}{L}\right) \right] \left(\cos\left(\frac{2x_3}{L}\right) + 2 \right), \quad (59)$$

where ρ_0 , V_0 and L are used as nondimensionalization constants. For these simulations ρ_0 and p_0 are set to 1 and $1/\gamma$, respectively. Additionally, V_0 is used as a parameter that controls the initial fluctuation Mach number $M_t = V_0/\sqrt{\gamma p_0/\rho_0}$ and, therefore, the compressibility effects. The Reynolds number $Re = \rho_0 V_0 L/\mu_0$ is set to 5000, independently of the chosen Mach number.

Initially, a low Mach number $M_t = 0.1$ is chosen to avoid compressibility effects and compare the QSV-LES method against the Smagorinsky model (Smagorinsky, 1963b) the Dynamic procedure (Germano et al., 1991; Lilly, 1992b) and the Coherent vorticity Preserving (CvP) method (Chapelier et al., 2018), which have been developed in contexts limited to incompressible turbulence.

Before a direct comparison between models is made though, data from a Direct Numerical Simulation (DNS) performed with 384^3 grid points at the same initial conditions is used to directly evaluate the spectral content of the sub-filter stress tensor τ_{ij} , i.e. how much energy flows through the sharp spectral grid cutoff for each wavenumber. These results are then compared in figure 6 against the outcome of the QSV model if applied to sharp-spectrally filtered DNS data with grid cutoff $k_c = 48$.

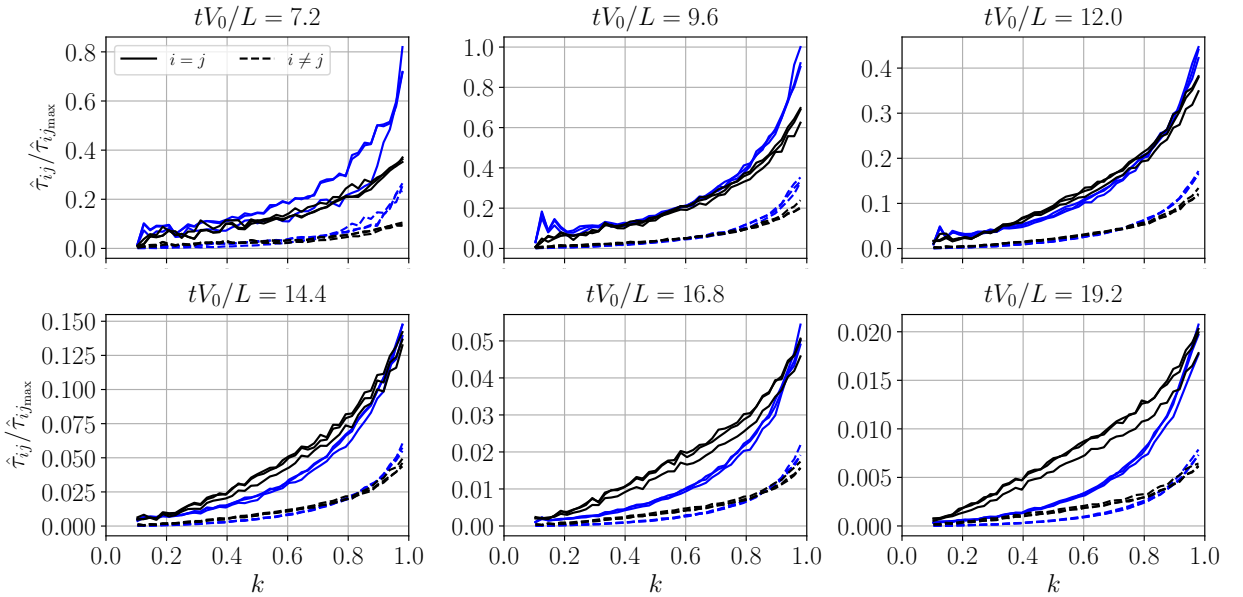


Fig. 6: Exact sub-filter stress tensor, $\hat{\tau}$, extracted from a DNS of the Taylor Green Vortex (blue) with initial amplitude of $V_0 = 0.1$ at various instants is compared against the *a priori* $\hat{\tau}$ predicted by the QSV approach when applied to sharp-spectrally filtered DNS data with grid cutoff $k_c = 48$ (black).

Figure 6 shows the evolution of the different components of the SFS tensor at various instants as the initial vortex breaks down and, by doing so, it displays the existence of a distinct behavior between the trace and off-diagonal components after an initial transient. The components that belong to the trace have a higher magnitude for all wavenumbers up to k_c when compared to τ_{12} , τ_{13} , τ_{23} .

In incompressible solvers, the trace of the SFS is generally absorbed into the so-called “modified pressure” and its value is determined by the divergence free flow constraint given by the conservation of mass. In a compressible setting, pressure is a thermodynamic quantity coupled with density and temperature, making this procedure not possible. In order to account for the different spectral behavior between the diagonal and off-diagonal components of τ_{ij} , the coefficient ($C_{\tau_{ij}}$) is set to 0.6 when $i \neq j$ and is maintained at 1.0 for the trace components when modeling τ_{ij} , as discussed in the end of section 4.

After this adaptation, the results acquired from the model for the different components of τ_{ij} are shown in black in figure 6. It can be seen that as the flow is breaking down and turbulence is developing the QSV model under predicts the value of the energy at the cutoff, responsible for introducing the magnitude the magnitude of the $\hat{\tau}_{ij}$ components but, as the flow develops, the “plateau-cusp” behavior is accurately introduced by the model, which follows closely the directly calculated values. Ultimately, near the end of the simulation, some degree of over dissipation in the middle wavenumber range is introduced but the correct magnitude at the cutoff is kept.

The state of the turbulence of the TGV is monitored by analyzing the evolution of volume-averaged kinetic energy, $E_{\text{kin}} = \langle \frac{1}{2} u^2 \rangle$ and its dissipation rate, defined as,

$$\epsilon_{\text{kin}} = -\frac{\partial E_{\text{kin}}}{\partial t}. \quad (60)$$

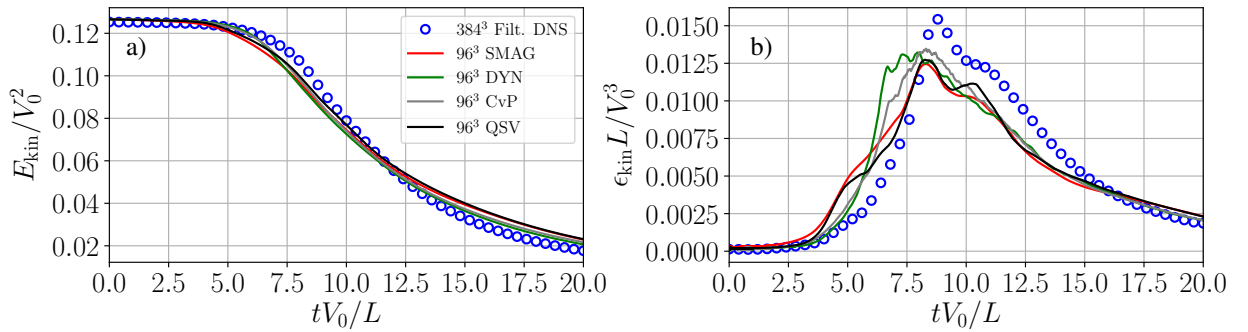


Fig. 7: Evolution of total energy (a) and dissipation (b) of the LES of the Taylor-Green Vortex with initial amplitude of $V_0 = 0.1$. Different subfilter models are shown and compared against DNS data.

Figure 7 gathers the behavior of the kinetic energy and its dissipation in the simulation of a TGV with different LES models and with a DNS approach. It can be observed that QSV’s behavior is similar to the plain Smagorinsky model but, at any given time, it is closer to the filtered DNS dissipation curves. The current model, therefore, outperforms Smagorinsky by introducing lower dissipation levels in the beginning and higher levels after the dissipation’s peak in the breakdown simulations. Moreover, the Dynamic procedure and the CvP method are capable of decreasing the dissipation rate in the initial stages and delaying the initial breakdown, unlike Smagorinsky or QSV, following the DNS data more closely initially, however they miss the dissipation plateau after the peak and introduce much higher dissipation levels around $tV_0/L = 6.0$.

A grid convergence study is performed on the QSV LES of a TGV at $M_t = 0.1$ and $Re = 5000$ and the results are gathered in figure 8. At each grid resolution the results are compared against the energy and dissipation of DNS data spectrally filtered to match the LES grid. The results show that each increase in resolution induces an improvement in the predicted time evolution of the simulated energy and dissipation in both delaying the initial breakdown and introducing a dissipation plateau after the initial peak.

After the results on nearly incompressible flow are established, a higher initial Mach number of $M_t = 1.2$ is tested. At this level, the initial perturbations rapidly induce wave steepening and shocks (see figure 9) in the solution before

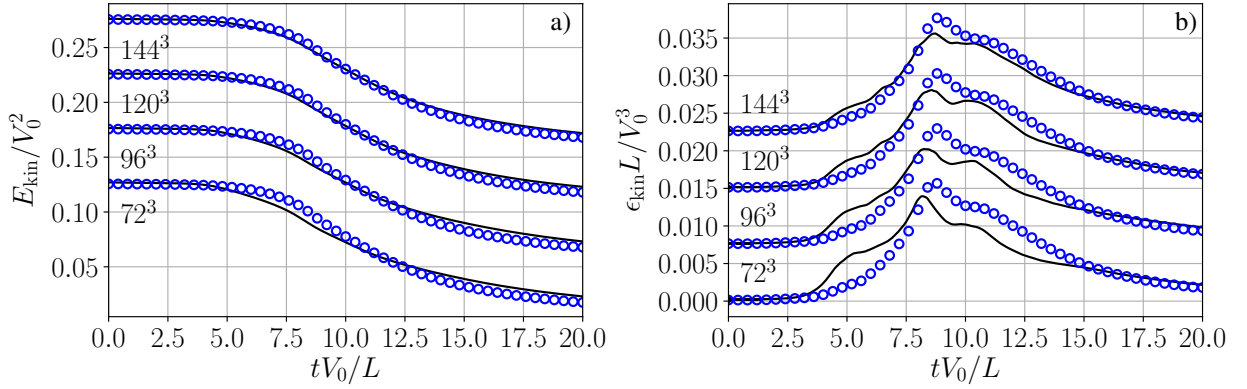


Fig. 8: Grid convergence study for the QSV LES of a TGV at $M_t = 0.1$ and $Re = 5000$. Displayed are the evolution of total energy (a) and dissipation (b) for 72^3 , 96^3 , 120^3 and 144^3 grid points compared against the results acquired from a sharp spectral filtered DNS up to the same cutoff. Results are vertically shifted for clarity.

the initial vortex breaks down into turbulence and the hydrodynamics start to govern the flow. The objective of this test case is to assess how the different models cope with the presence of both shocks and turbulence in the same flow.

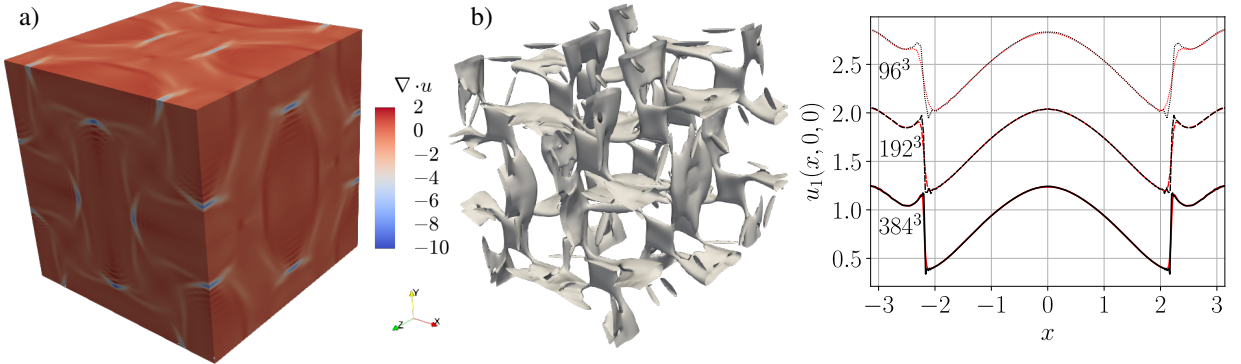


Fig. 9: Visualization of a 96^3 simulation of a TGV with $M_t = 1.2$ and $Re = 5000$ at time $tV_0/L = 6.75$ displaying divergence field contours (a) and its isosurfaces at $\nabla \cdot \mathbf{u} = -0.5$ (b) is shown on the left together with the velocity field at the centerline at different grid resolutions for both QSV (black) and LAD augmented Smagorinsky (red), on the right.

Previously, though, the concept of a compressible energy norm will be introduced since there is need to extend the kinetic energy notion, used in incompressible flows to monitor turbulence, to setups in which the compressibility effects are important. With the objective of investigating the possibility of measuring acoustic power transmission directly in convoluted flows, Myers (1991) derived an exact equation governing the energy transported by fluctuations of arbitrary steady base flows. The derived exact energy norm is

$$E_{nl} = \rho [(H - H_0) - T_0(s - s_0)] - \rho_0 \mathbf{u}_0 \cdot (\mathbf{u} - \mathbf{u}_0) - (p - p_0), \quad (61)$$

where H is the total enthalpy, s is the entropy and the subscript $_0$ is used to indicate base state quantities, which are the initial flow quantities in the current case. This result is generic and encompasses perturbations up to any order. Following, E_{nl} can be restricted to first order, i.e. linear, fluctuation dynamics with the help of thermodynamic

relations, which leads to

$$E_{\text{lin}} = \frac{p_1^2}{2\rho_0 c_0^2} + \frac{1}{2}\rho_0 \mathbf{u}_1^2 + \rho_1(\mathbf{u}_0 \cdot \mathbf{u}_1) + \frac{\rho_0 T_0 s_1^2}{2c_{p_0}}. \quad (62)$$

Additionally, in the case of the TGV, the base flow velocity field is identically zero ($\mathbf{u}_0 = 0$) and the relations above can be reduced to

$$E_{\text{nl}} = \rho(h - h_0) + \frac{1}{2}\rho \mathbf{u}^2 - \rho T_0(s - s_0) - (p - p_0), \quad (63)$$

$$E_{\text{lin}} = \frac{p_1^2}{2\rho_0 c_0^2} + \frac{1}{2}\rho_0 \mathbf{u}_1^2 + \frac{\rho_0 T_0 s_1^2}{2c_{p_0}}. \quad (64)$$

Note that, for the case where $M_t = 0.1$, the compressibility effects can be neglected and the energy norms reduce to the nonlinear and linear kinetic energy norms, respectively.

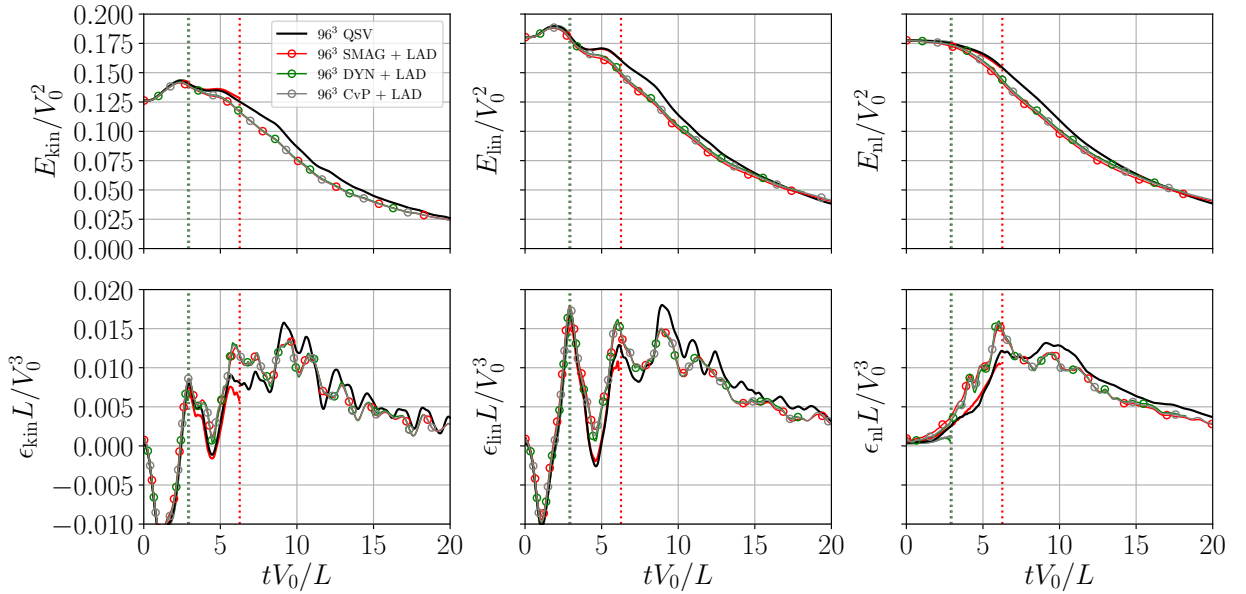


Fig. 10: Evolution of energy norms and their dissipation in the LES of the Taylor-Green Vortex with initial amplitude of $V_0 = 1.2$. Different subfilter models are shown. By themselves, the Smagorinsky, CvP and Dynamic models lead to unstable simulations and their blowup time is shown in dotted lines (\cdots). These models were then augmented with the LAD shock capturing.

Figure 10 gathers the evolution of the three different energy norms, E_{kin} , E_{lin} and E_{nl} , as well as their dissipation for the TGV with $M_t = 1.2$ and $Re = 5000$. It can be observed that both E_{kin} and E_{lin} display a non-monotonic behavior with an initial energy “growth” and a “negative dissipation”. Since there is no actual energy being added to the system, this behavior actually indicates that there is energy transfer from other components that are not accounted for in E_{kin} and E_{lin} . In the kinetic energy case, the lack of accounting for the energy stored in the thermodynamic fields explains where the “extra” energy necessary for the growth shown in figure 10 comes from. For E_{lin} , though, the difference is more subtle. E_{lin} accounts for perturbations in both hydrodynamic and thermodynamic fields but only up to first order, therefore, only relatively low amplitude oscillations can be accurately characterized by this energy norm. Figure 10

shows, though, that difference between the linear and nonlinear norms is considerable in the early stages of the flow. Being TGV with $M_t = 1.2$ being both compressible and nonlinear the full energy exact norm, E_{nl} , is necessary to accurately display the dynamics of this flow. It can be seen that, by using this norm, positiveness of the energy dissipation is preserved.

Figure 10 also shows that the Smagorinsky, CvP and Dynamic models, by themselves, lead to unstable simulations when the supersonic initial condition of $V_0 = 1.2$ is used. On the other hand, if these models are augmented by the use of a separate shock capturing technique, such as the LAD, the overall dissipation is much higher than the predicted by the QSV model. A grid sensitivity analysis is also performed and the results are gathered in figure 11. Such results indicate that the accuracy of the QSV method at coarse resolutions is much higher than when the LAD method is combined with a classic LES model. In fact, the results in the right plot of figure 10 show that at least 2 times more grid points in each direction are necessary by the latter technique to achieve a similar accuracy level as the QSV approach.

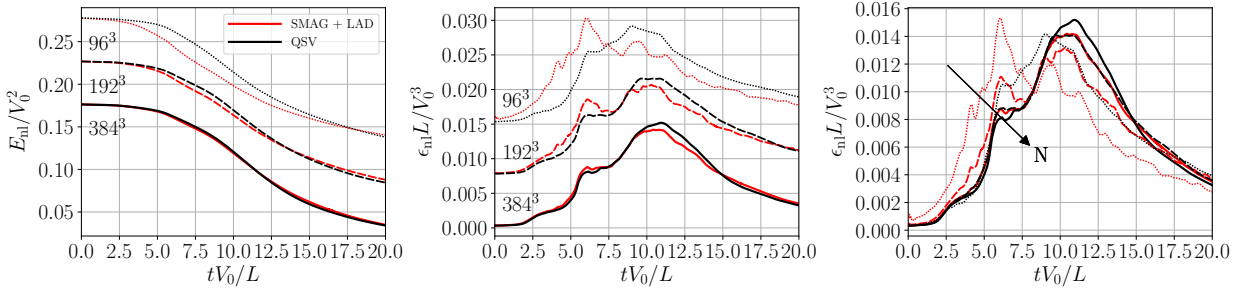


Fig. 11: Evolution of nonlinear energy norm and its dissipation in the Taylor-Green Vortex simulation with initial amplitude of $V_0 = 1.2$ at different grid resolution levels. Results are shown comparing the QSV model (black) with the Smagorinsky model coupled with LAD shock capturing (red).

5.3. Two Dimensional Inviscid Strong Vortex/Shock-Wave Interaction

A stationary shock sustained by an inflow velocity of $V_0 = 1.5 \sqrt{\gamma p_0 / \rho_0}$ is initialized at $x_s = L/2$ inside a computational domain $\Omega = [0, 2L] \times [0, L]$. Superposed to this base state, a compressible zero-circulation vortex is initialized upstream of the shock at $(x_v, y_v) = (L/4, L/2)$ with an inner core radius equal to $a = 0.075L$ and an external radius $b = 0.175L$. This can be translated as $\mathbf{u} = u_\theta(r)\hat{\mathbf{e}}_\theta + V_0\hat{\mathbf{e}}_x$, where r is the radial distance from the center of the vortex and

$$\frac{u_\theta(r)}{u_\theta(a)} = \begin{cases} \frac{r}{a}, & \text{if } r \leq a \\ \frac{\eta}{2} \left(\frac{r}{b} - \frac{b}{r} \right), & \text{if } a < r \leq b \\ 0, & \text{otherwise,} \end{cases} \quad (65)$$

where $\eta = 2(b/a)/[1 - (b/a)^2]$ and the maximum tangential velocity is set to $u_\theta(a) = 0.9V_0$. Following the pressure field is initialized so that its gradient balances the centripetal force and the following system of equations is solved based on the ideal gas relation and isentropic compression,

$$\frac{\partial P}{\partial r} = \rho \frac{u_\theta^2(r)}{r}, \quad P = \rho RT, \quad \frac{P}{P_0} = \left(\frac{\rho}{\rho_0} \right)^\gamma. \quad (66)$$

Such a setup was previously introduced by Ellzey et al. (1995) to study the structure of the acoustic field generated by the shock-vortex interaction, by Rault et al. (2003) to analyze the driving mechanisms for the production of vorticity in the interaction at high Mach Numbers and by Tonicello et al. (2020) to investigate shock capturing techniques in high-order methods focused on their influence on the entropy field and its non monotonic profile across a shock.

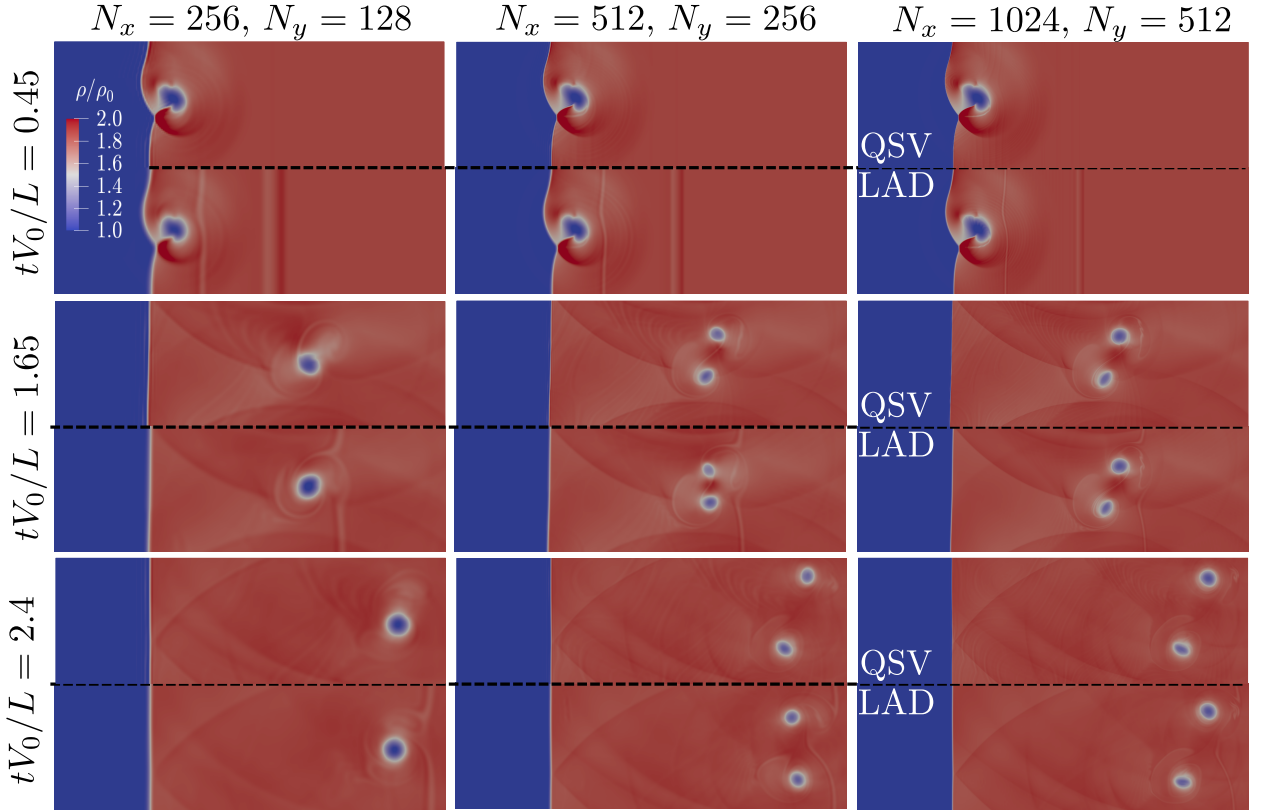


Fig. 12: Density isocontours of an inviscid shock/vortex interaction at different grid resolutions for both Local Artificial Diffusivity (LAD) shock capturing method and for the filter modulated spectral viscosity method.

In the current work, this setup is used to assess the accuracy of the proposed Quasi-Spectral Viscosity (QSV) method. With that objective, the inviscid shock/vortex interaction was solved at 3 different grid resolution levels, $N_x = 256; N_y = 128$, $N_x = 512; N_y = 256$ and $N_x = 1024; N_y = 512$, using both QSV and the LAD shock capturing scheme (Kawai et al., 2010), being the results gathered in figure 12. The outcome shows that at the highest resolution level, both methods converge qualitatively to a similar result, which indicates a post shock vortex separation with the bottom vortex trailing its top counterpart. By analyzing the results from the intermediate and coarser grid resolution levels, though, one is able to conclude that the QSV model converges faster than the LAD method. Although both models suppressed the vortex breakdown at the coarsest resolution and predicted their separation at the intermediate grid, their correct relative displacement is only recovered by the simulation with the QSV model.

Following, the original computational domain for the shock-wave/vortex interaction test case, $\Omega = [0, 2L] \times [0, L]$,

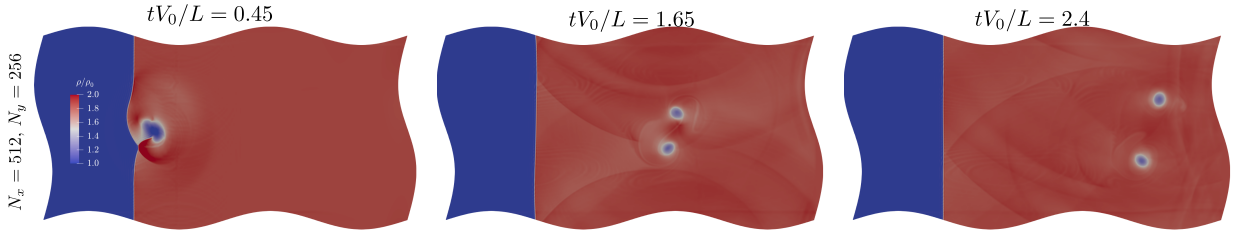


Fig. 13: Density isocontours of an inviscid shock/vortex interaction using a distorted wavy grid and the Quasi-Spectral Viscosity (QSV) method.

was distorted by adding a sinusoidal component in both directions where the following linear mapping,

$$(x_d, y_d) = \left(x + 0.05L \sin\left(\frac{2\pi}{L}y\right), y + 0.05L \sin\left(\frac{2\pi}{L}x\right) \right) \quad (67)$$

relates the original (x, y) to the distorted grid (x_d, y_d) . To solve the compressible Navier-Stokes system of equations with the added closure terms from the QSV model in such a nonorthogonal grid, a curvilinear grid transformation such as in Nagarajan et al. (2007), was used. The full grid transformed equations and sub filter models are gathered in Appendix C. Figure 13 shows that QSV model is capable of both sustaining the shock and producing qualitatively accurate results even in distorted grids.

5.4. Two Dimensional Sinusoidal Wall/Shock-Wave Interaction

The reflection of a shock wave from a sinusoidal wall was chosen as a test case to assess how the QSV model behaves in the presence of solid boundaries. The setup is built with the objective to mimic experiments reported by Denet et al. (2015), where a planar shock wave impinges on a sinusoidal wall with 1.0 mm amplitude and wavelength of 2.0 cm. Following Tonicello et al. (2020), a computational domain encompassing one wavelength and 10 cm in the wall normal direction is used for two numerical experiments. The first is a $M = 1.5$ shock propagating in air ($\gamma = 1.4$), similar to the original experiments, and the second is a $M = 5.0$ shock propagating in a fluid with a lower specific heat ratio of $\gamma = 1.15$, which increases the strength of the reflected shock and approaches the Newtonian limit (Lodato et al., 2017). The simulations are solved with periodic conditions at the top and bottom boundaries together with a no slip adiabatic wall on the left. Moreover, this test case confirms the capability of the QSV model to solve the filtered equations in distorted grids.

The shock is initialized 7.5 cm away from the wall with left and right states corresponding to

$$\rho = \begin{cases} \rho_l = 1.208 \text{ kg m}^{-3}, \\ \rho_r = \rho_l \frac{(\gamma+1)M^2}{(2+(\gamma-1)M^2)}, \end{cases} \quad u = \begin{cases} u_l = 0.0 \text{ m s}^{-1}, \\ u_r = a_r \sqrt{\frac{(\gamma-1)M^2+2}{2\gamma M^2-(\gamma-1)}} - a_l M, \end{cases} \quad p = \begin{cases} p_l = 101.325 \text{ kPa}, \\ p_r = p_l \frac{2\gamma M^2-(\gamma-1)}{\gamma+1}, \end{cases} \quad (68)$$

where $a_{l,r} = \sqrt{\gamma \frac{p_{l,r}}{\rho_{l,r}}}$ is the speed of sound in either the left or right states. In both simulations the Sutherland's law for air was used to model dynamic viscosity. Since the lower Mach number test case, in comparison with the shock reflection near the Newtonian limit, leads to less complex reflection patterns and vortical features, it will be used only as a qualitative assessment and compared against previous experimental (Denet et al., 2015) and numerical (Lodato et al., 2016; Tonicello et al., 2020) results. Following, the $M = 5.0$ will be used to analyze the QSV model capability of solving such a flow setup.

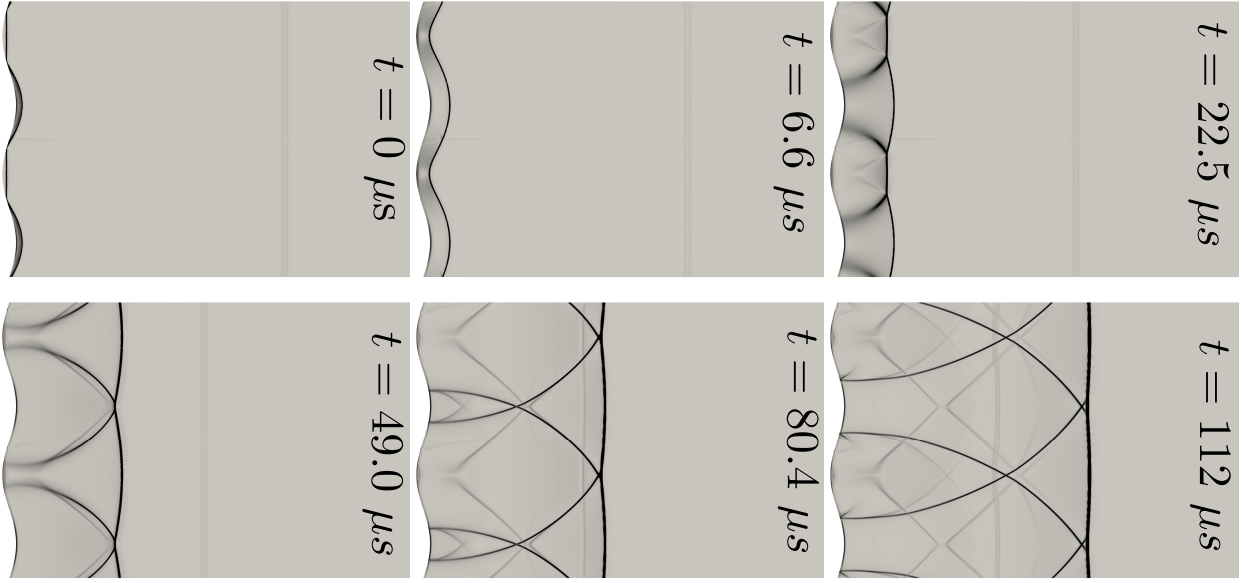


Fig. 14: Numerical Schlieren visualization of the patterns created by a $M = 1.5$ shock reflection off a sinusoidal wall achieved by performing a QSV simulation.

Figure 14 gathers the results of the simulation of the reflection of the $M = 1.5$ shock reflection when solved with the addition of the QSV in a mesh with 1024 points in the wall normal direction and 256 points in the tangential direction. Although a hyperbolic stretched grid was used to concentrate the resolution near the wavy wall, the current resolution is 8 times less fine in terms of degrees of freedom when compared with the simulations presented in Tonicello et al. (2020), for this case. Despite the lower resolution, the results qualitatively agree with previous experimental and numerical literature.

Following, the shock reflection near the Newtonian limit is performed with different grid resolutions. The results gathered in figure 15 show that the QSV model is capable of predicting the motion of the large scales of the flow even at low resolution. As the grid is refined, smaller and smaller vortical scales are resolved and the flow's complex pattern is accurately captured. Again, less degrees of freedom were necessary to achieve qualitatively similar results in comparison with simulations presented in Tonicello et al. (2020). For the shock/sinusoidal-wall reflection near the Newtonian limit about half of the degrees of freedom were used.

5.5. High-Speed Turbulent Channel Flow

The assessment of the QSVmodel in presence of solid boundaries is tackled further via compressible turbulent channel flow simulations at supersonic and hypersonic bulk Mach numbers, $M_b = 1.5$ and 6.0, respectively. Flow parameters are non-dimensionalized using the channel's half-width (δ), the speed of sound at the wall (a_w), the wall temperature (T_w) and the bulk density,

$$\rho_b = \langle \rho \rangle_\Omega, \quad (69)$$

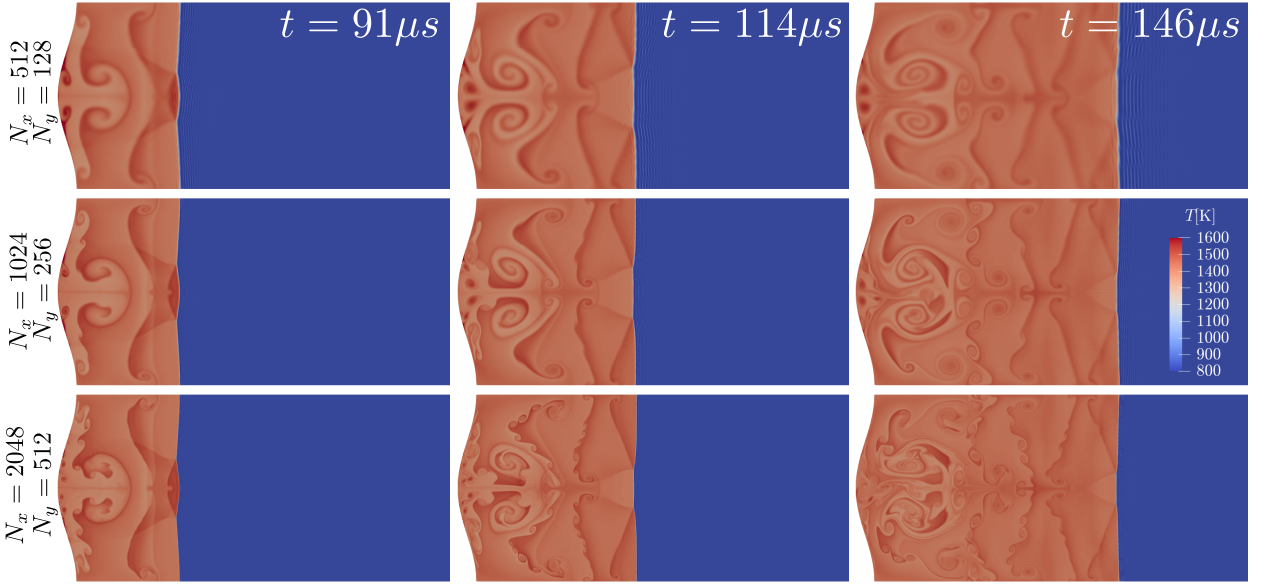


Fig. 15: Temperature isocontours visualization of the patterns created by a $M = 5.0$ shock in a fluid with $\gamma = 1.15$ after it is reflected off a sinusoidal wall at different grid resolutions performed via a QSV simulation.

where the bracket $\langle \cdot \rangle_\Omega$ represents the volume average over the computational domain. The bulk Reynolds number

$$Re_b = \frac{\rho_b U_b \delta}{\mu_{\text{ref}}}, \quad (70)$$

is also assigned, where U_b is the bulk velocity defined as $U_b = \langle \rho u_1 \rangle_\Omega / \rho_b$ and where μ_{ref} is the reference dynamic viscosity at the wall. Additionally, the bulk Mach number can be defined in terms of the aforementioned scales as $M_b = U_b / a_w$ and a power law given by

$$\frac{\mu}{\mu_{\text{ref}}} = \left(\frac{T}{T_{\text{ref}}} \right)^n, \quad (71)$$

with $n = 0.76$ is assumed for the dynamic viscosity.

The flow settings are inspired in the work of Chen and Scalo (2021) who, for a given M_b , adjusted the value of Re_b so that the friction-based Reynolds number that accounts for variable density effects (Huang et al., 1995),

$$Re_\tau^* = \frac{\bar{\rho}(\delta) \sqrt{\tau_w / \bar{\rho}(\delta)}}{\bar{\mu}(\delta)} \delta, \quad (72)$$

would remain approximately constant for each grid resolution level. Although table 2 shows that this is achieved by the current setup, the coarse resolutions considered in this manuscript, chosen to put the turbulence closures performance to test, are not sufficient to recover the DNS-predicted $Re_\tau^* \approx 220$ reported in the work of Chen and Scalo (2021). As the grid is refined, though, the difference between the values recored by the current simulation and the DNS gets smaller.

High-speed turbulent channel flow calculations were performed using the parameters collected in table 2 with both the eddy-viscosity model proposed by Vreman (2004) and the QSV approach as the turbulence closure. Results

M_b	Re_b	$L_x \times L_y \times L_z$	$N_x \times N_y \times N_z$	Re_τ	Δx^+	Δy_{\min}^+	Δz^+	Re_τ^*
1.5	5000	$12\delta \times 2\delta \times 4\delta$	$32 \times 72 \times 16$	258	99	0.29	68	162
			$64 \times 108 \times 32$	300	57	0.22	38	193
			$128 \times 160 \times 64$	325	30	0.16	20	213
6.0	20000	$16\delta \times 2\delta \times 4\delta$	$80 \times 90 \times 40$	2270	460	2.0	232	164
			$160 \times 135 \times 80$	2500	251	1.5	126	195
			$320 \times 200 \times 160$	2640	132	1.0	66	212

Table 2: Parameters for the turbulent channel simulations performed in the current work.

for the transformed mean velocity

$$U_{TL}^+ = \int_0^{\bar{U}/u_\tau} \left(\frac{\bar{\rho}}{\rho_w} \right)^{1/2} \left[1 + \frac{1}{2} \frac{1}{\bar{\rho}} \frac{\partial \bar{\rho}}{\partial y} y - \frac{1}{\bar{\mu}} \frac{\partial \bar{\mu}}{\partial y} y \right] d(\bar{U}/u_\tau), \quad (73)$$

plotted against the semi-local wall coordinate (Morkovin, 1962; Huang et al., 1995),

$$y^* = \frac{\bar{\rho}(y)u_\tau^*}{\bar{\mu}(y)}y, \quad \text{where} \quad u_\tau^* = \sqrt{\tau_w/\bar{\rho}(y)}, \quad (74)$$

are used to assess the performance of each model. This velocity transformation was introduced by Trettel and Larsson (2016) to account for both variable density and heat transfer effects, which are non-negligible in the current setup.

Figure 16 shows that both models at all grid resolution levels are able to capture the correct viscous sublayer scaling. The performance difference between the models is observed in the logarithmic region, where, at each grid resolution level, the Vreman's model is closer than QSV to the reference log-law profile,

$$U^+ = \frac{1}{\kappa} \ln(y^*) + C \quad \text{where} \quad C = 5.5 \quad \text{and} \quad \kappa = 0.41. \quad (75)$$

Nonetheless, the QSV model's predictions for the transformed mean velocity profiles are not far from the ones by Vreman's model and, moreover, as the grid is refined, convergence is observed. This result shows that the QSV approach is also applicable to wall-bounded turbulent flows, opening the possibility of future simulations of shock/boundary-layer interaction simulations using a single model for both the effects caused by shocks and turbulence.

6. Conclusion

A novel technique named the Quasi-Spectral Viscosity model (QSV), was introduced. It is designed to simulate accurately the large scales present in both shock and turbulence dominated flows by exploiting the residual of filter transfer functions to estimate both the amplitude of fluctuations near the grid cutoff and modulate the viscosity magnitude for different wavenumbers. This feature allows for an implementation using only spatial operators, ideal for inhomogeneous flows.

The QSV mathematical framework is based on an extension of LES closures and a parallel between these and spectral vanishing viscosity (SVV) based models. The 1D Burgers' problem is used to showcase the connection between previous LES models and how they can be as a way of solving shock dominated solutions. Moreover, although the SVV model has been shown to work well when solving equations that allow discontinuous solutions (Tadmor,

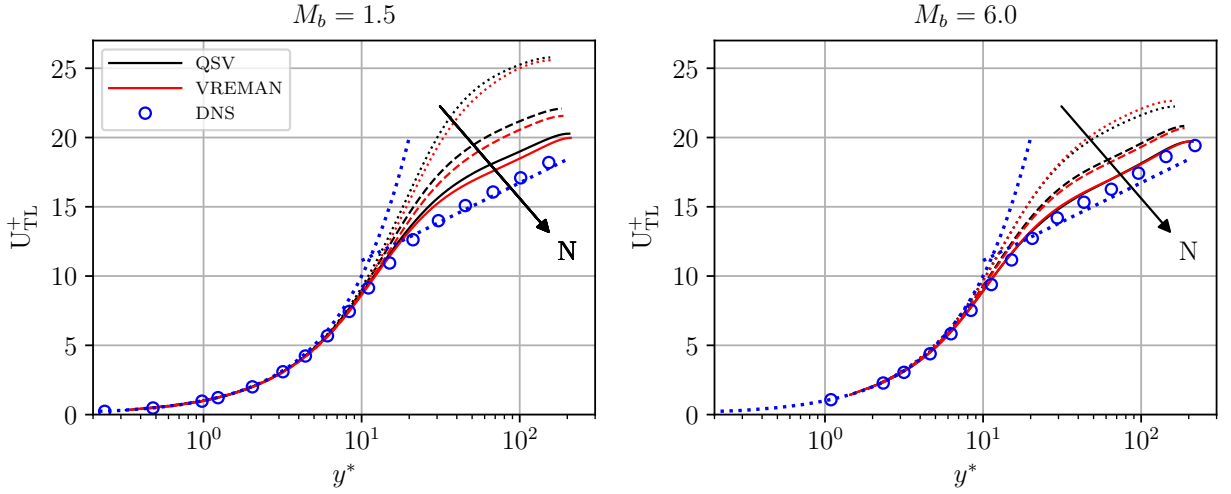


Fig. 16: Transformed mean velocity profiles for high-speed channel simulations at different bulk Mach numbers and grid resolutions. As the grid is refined, the line style becomes denser, going from dotted to solid. The simulations were performed using the Vreman (2004) and QSV methods. Reference values for the viscous sublayer and the logarithm region are shown in blue dotted lines and DNS data from Chen and Scalò (2021) is shown in blue symbols. See table 2 for a complete description of the simulation parameters.

1989, 1990), a mathematical justification explaining its extension to turbulent flows (Karamanos and Karniadakis, 2000; Pasquetti, 2006) was missing. The reasons are presented in the current manuscript in section 2: The grid filter introduces the need for an energy flux to sub-filter scales that affects all resolved wavenumbers and peaks at near the cutoff. The SVV kernel, although being inviscid for low wavenumbers, also peaks near the cutoff and can be considered a first order estimate of the exact sub filter flux needed.

Moving forward, the QSV model was tested in one-, two- and three-dimensional problems of increasing complexity and it is shown the perform well in both low-speed and highly compressible flow setups. For example, the same QSV framework can be used to solve a Taylor-Green Vortex with both sub and supersonic initial conditions. Moreover, the QSV model is flexible, being able to be applied in curved and stretched domains by using grid transformations. The collection of satisfactory results across intrinsically different flow setups supports the claim that the QSV method can simultaneously capture shocks and act as sub-filter turbulent closure.

As a final remark, although the current implementation is aimed at finite difference solvers, it is possible to extend the QSV approach to solvers based on spectral elements or even Discontinuous Galerkin formulations, as pointed out in the manuscript. Not only it would be possible, but it would also be simpler. A spectrally based implementation would be able to easily gage the magnitude of the oscillations near the cutoff and would be able to modulate freely the amplitude of the viscosity kernel for different wavenumbers. The authors encourage future development in this direction.

Appendix A. QSV-inspired 1D Legendre-Galerkin Simulations

As previously discussed, the extension of the current method to any hierarchical set of basis functions is straightforward. Following, the Sod shock tube and Shu-Osher shock-entropy wave interaction canonical problems are revis-

ited using a Legendre-Galerkin based discretization and proof of concept results are presented. The 1D Euler system of equations augmented by the models for the SFS flux terms discussed in subsection 5.1, with

$$\tau_{11} = -\bar{\Delta} \sqrt{k_c E_{uu}(k_c)} \left[\left(1 - \tilde{G}_{\text{eff}}(\alpha, \beta, w) \right) * \frac{\partial \check{u}_1}{\partial x_1} \right], \quad (\text{A.1})$$

$$q_1 = -0.6\bar{\Delta} \sqrt{k_c E_{uu}(k_c)} \left[\left(1 - \tilde{G}_{\text{eff}}(\alpha, \beta, w) \right) * \frac{\partial \check{T}}{\partial x_1} \right], \quad (\text{A.2})$$

$$(\text{A.3})$$

is solved with a fourth order Runge-Kutta time advancement scheme. Being the energy at the cutoff a global operator and the grid spacing non uniform in this implementation it was preferred to separate the information on the length scale to the velocity field fluctuations scale.

As previously, the effective filter transfer function \tilde{G}_{eff} (34) is used to modulate the wavenumber response of the sub filter stress fluxes. The transfer function does not need to be based on Padé operators since this is a spectral implementation but, to allow a direct comparison against the spatial finite difference implementation, an equivalent filter transfer function was used with the same coefficients: the averaging coefficient of $\beta = 0.8$, the Padé filter strength of $\alpha = 0.45$ and the ‘DC’ offsets of $w = 0.85$ for τ_{11} and $w = 0.95$ for q_1 .

The spatial discretization is based on a Legendre spectral-collocation scheme, where the solution points are defined at the Gauss-Lobatto quadrature nodes (x_j). These points are chosen because they influence the stability of the system by efficiently expanding functions in a way which decreases the importance of the Runge’s phenomenon (Karniadakis and Sherwin, 2013). The spatial collocated derivative operator for the Legendre-Gauss-Lobatto points is defined as,

$$D_{ij} = \begin{cases} -\frac{N(N+1)}{4}, & \text{if } i = j = 0, \\ \frac{L_N(x_i)}{L_N(x_j)} \frac{1}{x_i - x_j}, & \text{if } i \neq j \text{ and } 0 \leq k, j \leq N, \\ 0, & \text{if } 1 \leq i = j \leq N - 1, \\ \frac{N(N+1)}{4}, & \text{if } i = j = N. \end{cases} \quad (\text{A.4})$$

Following, the aforementioned quadrature nodes (x_j) are defined as being the zeros of $(1 - x^2)L'_N$, where L_N is the N-th order Legendre polynomial. Shen et al. (2011) describes an efficient algorithm to compute the location of the interior nodes of the Legendre-Gauss-Lobatto by finding the eigenvalues of the following matrix,

$$A_{N-1} = \begin{bmatrix} 0 & \sqrt{b_1} & & & \\ \sqrt{b_1} & 0 & \sqrt{b_2} & & \\ & \ddots & \ddots & \ddots & \\ & & \sqrt{b_{N-3}} & 0 & \sqrt{b_{N-2}} \\ & & & \sqrt{b_{N-2}} & 0 \end{bmatrix}, \quad (\text{A.5})$$

where,

$$b_j = \frac{j(j+2)}{(2j+1)(2j+3)}. \quad (\text{A.6})$$

In possession of the information on the node location, one can compute the weights of the quadrature points by the following formula,

$$w_j = \frac{2}{N(N+1)} \frac{1}{L_N^2(x_j)}. \quad (\text{A.7})$$

Ultimately, the knowledge of the quadrature nodes and weights is important to perform the projection onto the chosen hierarchical basis functions since the following operation,

$$\int_{-1}^1 p(x) dx = \sum_{j=0}^N p(x_j) w_j, \quad (\text{A.8})$$

holds for any polynomial that belongs to the polynomial space P up to order $2N - 1$. Therefore, an inner product between two polynomials u and v where their product belong to P can be exactly defined by the following discrete operation,

$$(u, v) = \int_{-1}^1 u(x)v(x) dx = \sum_{j=0}^N u(x_j)v(x_j)w_j, = \langle u, v \rangle_N. \quad (\text{A.9})$$

This operation can be used to project the solution fields onto a hierarchical set of basis functions and to find the energy at the cutoff as well as perform the any spectral filtering operation, such as the Vandeveen family of filters (Vandeveen, 1991).

At this point, one can use the Legendre polynomials directly to find the energy at the highest mode but, if no additional care is taken with the filtering operation, the difference between the filtered and unfiltered solution will lead to a formation of a boundary layer in the modeled sub filter stress flux terms. This happens because the projection operation also contains information on the boundary conditions and, upon filtering, some of this information is lost. To circumvent this issue, a combination of the initial Legendre polynomials,

$$\phi_k(x) = L_k(x) - L_{k+2}(x), \quad k = 0, \dots, N-2, \quad (\text{A.10})$$

such that the $N-2$ linearly independent functions automatically satisfy a homogeneous Dirichlet boundary condition. Now, the ϕ_k basis is made useful to non homogeneous settings by adding linear functions capable of lifting the solution,

$$\tilde{\phi} = \left\{ \frac{1-x}{2}, \frac{x+1}{2}, \phi_k \right\}. \quad (\text{A.11})$$

Now, if the filtering operation is performed only on ϕ_k , the attenuation of the oscillatory behavior is achieved and the boundary conditions are not affected.

The difficulty now is that, although $\tilde{\phi}$ is a linearly independent set of basis functions, it is not orthogonal. The amplitude of the different modes are found by solving a linear system that arises from using the Galerkin method as,

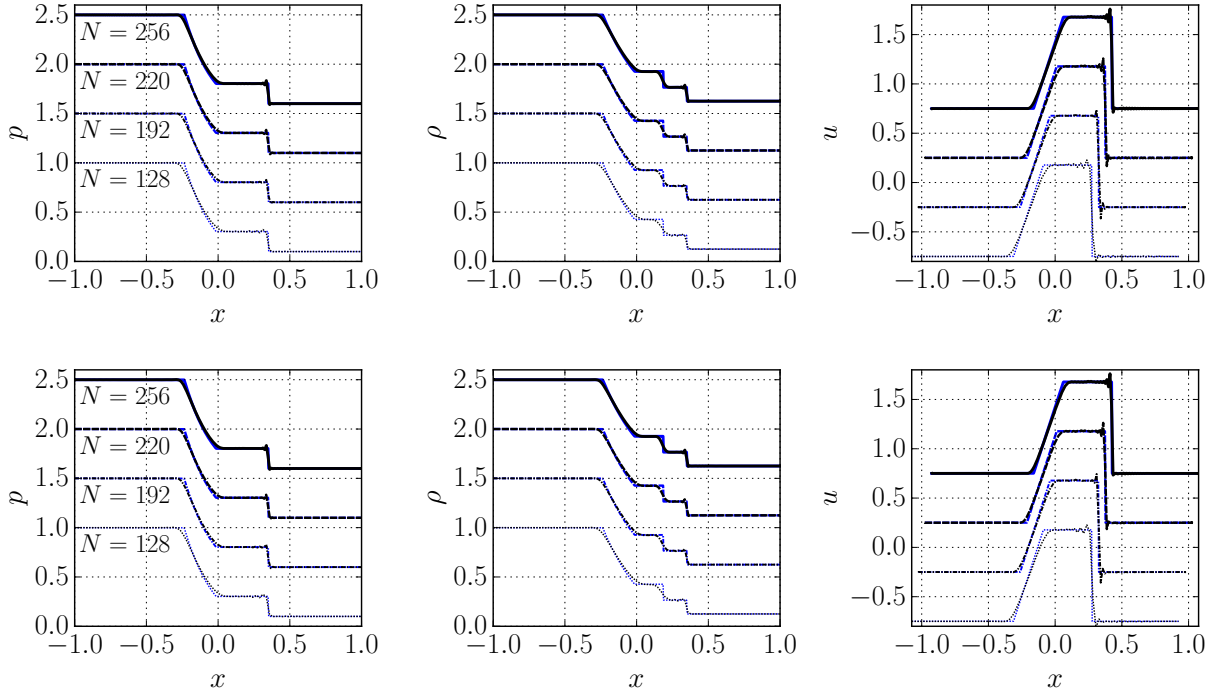


Fig. A.17: Sod shock tube results at $t = 0.2$ using a Legendre-Galerkin based discretization are compared with the analytical solution shown in solid blue lines without (top) and with (bottom) explicit filtering.

$$\langle \tilde{\phi}_i, \tilde{\phi}_j \rangle_N \cdot \hat{\mathbf{u}} = \langle u, \tilde{\phi}_j \rangle_N, \quad (\text{A.12})$$

$$\tilde{\mathcal{M}} \hat{\mathbf{u}} = \mathcal{F}, \quad (\text{A.13})$$

where the brackets represent the discrete inner product operation. Ultimately, the energy at the cutoff is found by getting the amplitude of the last mode applied to the kinetic energy field divided by the matrix norm of $\mathcal{M} = \langle \phi_i, \phi_j \rangle_N$. This last operation allows to compensate for the system being non-orthogonal and thus improve the estimate of the energy at the cutoff. These considerations allow for the implementation of the revisited spectral eddy viscosity model presented in the current work in a Legendre-Galerkin setting since now the spectral filtering and the energy at cutoff operations are defined.

Following, the Sod shock tube and Shu-Osher shock-entropy wave interaction problems were numerically simulated using the aforementioned discretization and the results of such computations are gathered in figures A.17 and A.18. By analyzing the outcomes, one can conclude that the model was successfully implemented in a Legendre-based spectral discretization. Although an explicit filtering step decreased the occurrence of spurious oscillations near the grid cutoff, the enhancement is marginal for both test cases. Results shown here are qualitatively similar to the 1D test cases performed by Maday et al. (1993).

In conclusion, the results presented serve as proof of concept that the method discussed in the current manuscript can be extended to different hierarchical basis functions and its implementation in a discrete Galerkin setting should

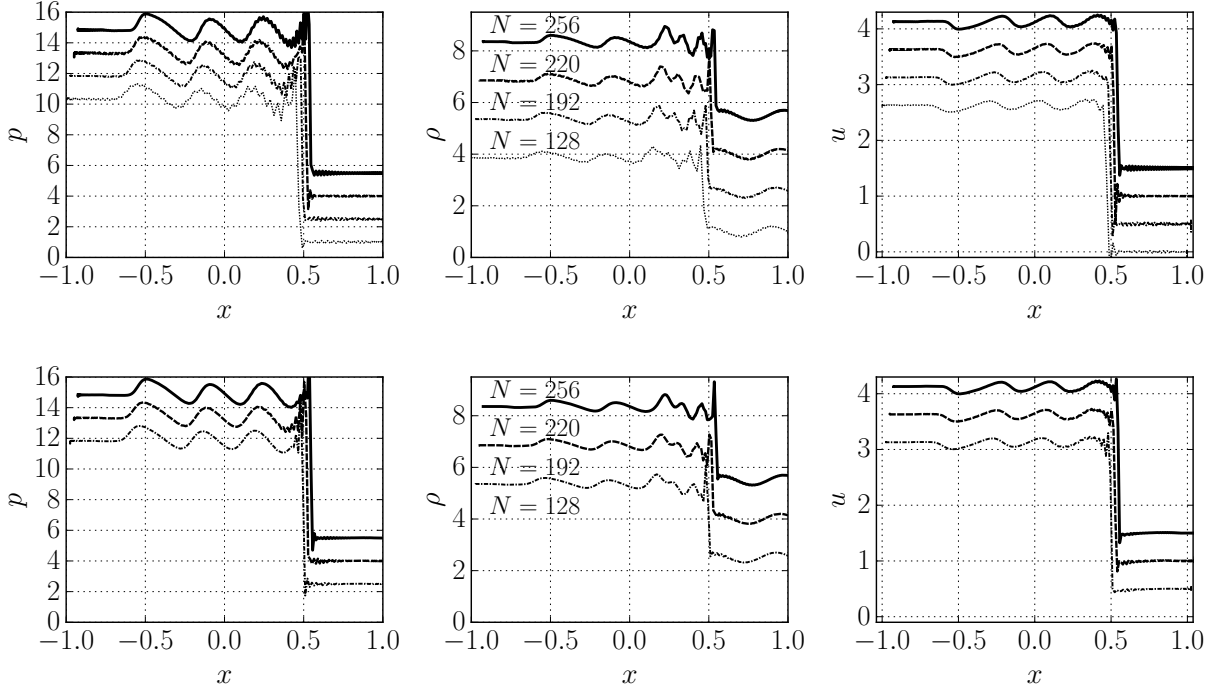


Fig. A.18: Shu-Osher shock entropy wave interaction results at $t = 0.36$ using a Legendre-Galerkin based discretization are shown at different grid refinement levels without (top) and with (bottom) explicit filtering.

be an interesting endeavor.

Appendix B. Closure for SFS Thermal Flux

In this section the Sod shock tube (Sod, 1978) is used as canonical *a priori* and *a posteriori* test case to inform the parameters used in the spectral modulation of the SFS Thermal Flux in the QSV approach.

The 1D Euler system of equations augmented by the models for the SFS flux terms discussed in subsection 5.1 will be solved using a Fourier based spatial discretization using a 4th-order Runge-Kutta time integration method. To be solvable by a Fourier method, two Riemann interfaces are initialized in the domain $x \in [-1, 1]$ with initial conditions,

$$[\rho, u, p](x, 0) = \begin{cases} [1, 0, 1], & \text{if } |x| < 0.5 \\ [0.125, 0, 0.1], & \text{otherwise.} \end{cases} \quad (\text{B.1})$$

This choice was preferred instead of using a direct cosine transform approach because the odd derivatives of the cosine basis functions are not directly represented by the initial orthogonal basis and a new projection operation would be needed. Moreover, the existence of the negative direction propagating shock, revealed important information during the *a priori* analysis.

The exact solution develops 4 states of constant density separated by a shock, a contact discontinuity and a rarefaction wave and it is shown in figure B.19 at time $t = 0.2$.

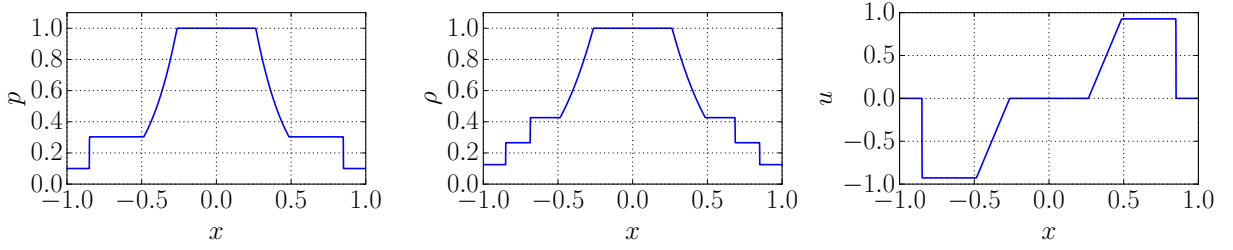


Fig. B.19: Exact solution of the Riemann shock tube (Sod, 1978) problem at dimensionless time $t = 0.2$.

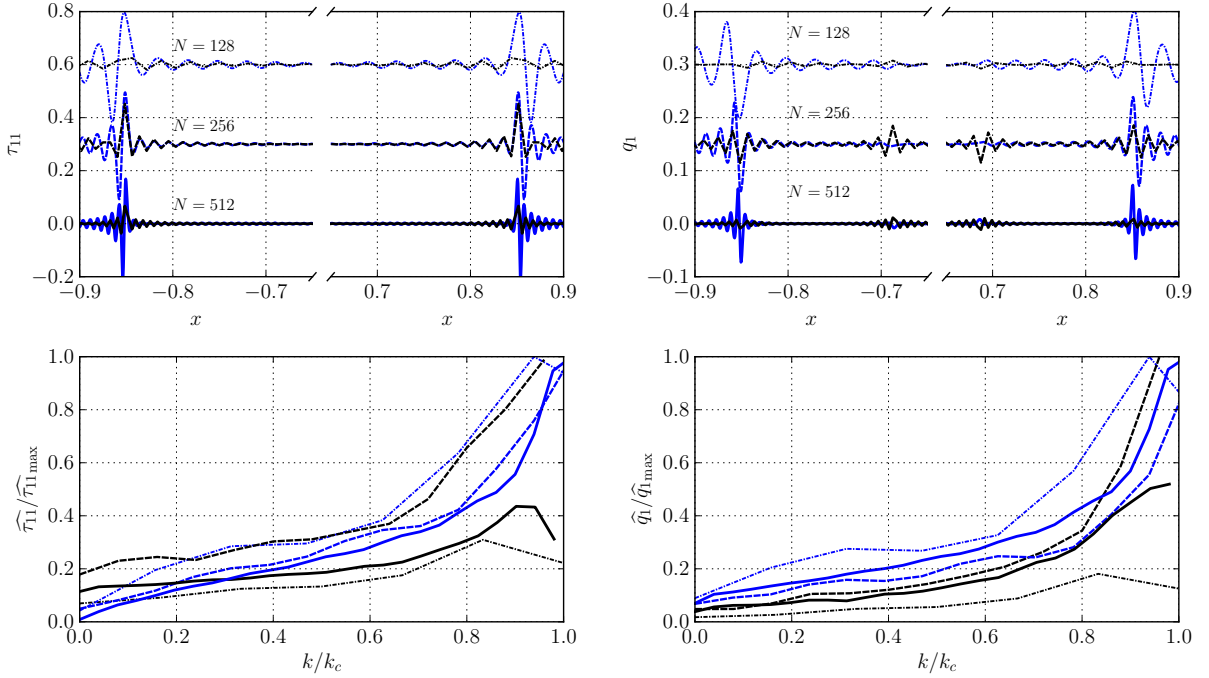


Fig. B.20: Energy flux to subfilter scales based on the exact solution of the Riemann shock tube (Sod, 1978) problem at $t = 0.2$ (blue) and the results achieved by the use of the proposed closure models (black).

The exact energy flux from large to small scales when a sharp spectral filter operation is performed was computed for $t = 0.2$ and such *a priori* results are shown in figure B.20 in blue. By examining these exact results some observations that help to inform the closure models can be performed. First, how the sign of the sub-filter quantities behaves whether the shock is moving in the positive or negative direction can inform the derivative of which resolved field quantity should be used in the closure model. Figure B.20 shows that τ_{11} maintains the sign independent of the shock propagation direction, on the other hand, q_1 changes its sign. Because of that, the derivative of the resolved temperature field is used to model q_1 , as opposed to derivatives of the resolved velocity field, which were used to model τ_{11} in the Burgers' simulations in section 2.

Using this information and dimensional analysis, the closure model for the SFS thermal flux is proposed to be augmented by a constant $C_q = 0.6$ as

$$q_1 = -C_q \sqrt{2\bar{\Delta}E_{uu}(k_c)} \left[\left(1 - \tilde{G}_{\text{eff}}(\alpha, \beta, w) \right) * \frac{\partial \tilde{T}}{\partial x_1} \right]. \quad (\text{B.2})$$

The constant was used to decrease its magnitude, found to be excessive in the *a priori* analysis, shown in figure B.20, if the constant was not present. Here, \tilde{G}_{eff} is effective filter transfer function (34) achieved by averaging the Padé and Fejér filters. Similarly as for τ_{11} , the values of the Padé filter strength, $\alpha = 0.45$, and the averaging coefficient, $\beta = 0.8$ were found to be satisfactory. The imposition of a ‘DC’ offset was also necessary for q_1 but a smaller shift of $w = 0.95$ led to better results.

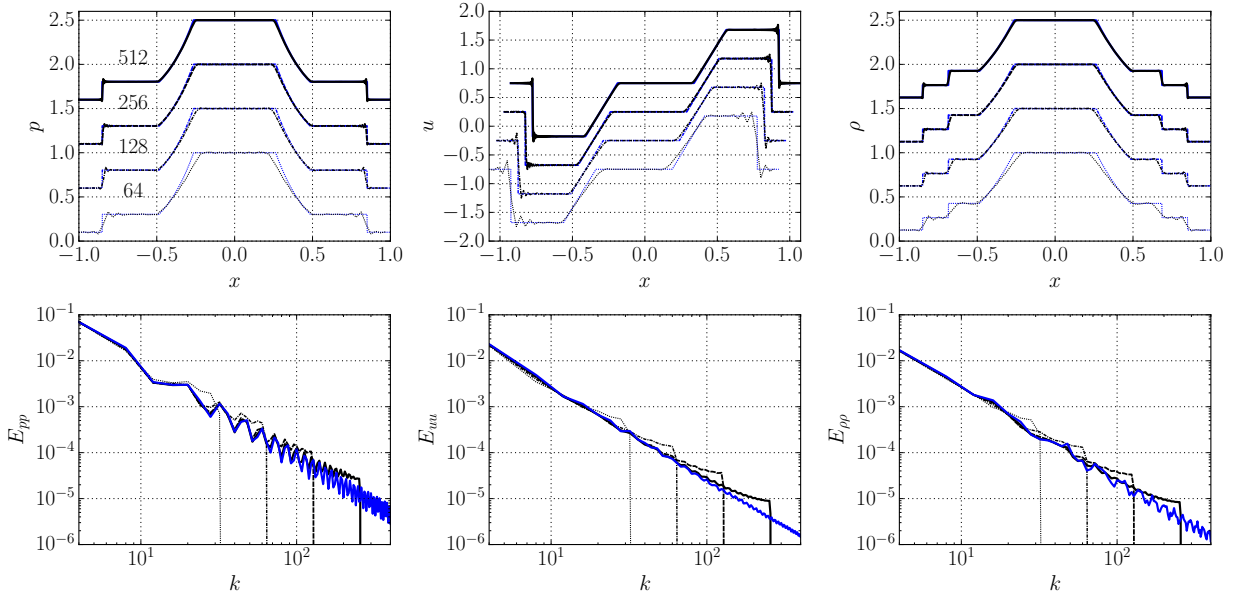


Fig. B.21: Pressure (left), velocity (center) and density (right) fields of Fourier based numerical simulation of mirrored 1D Riemann problem (black) is compared with its exact solution (blue) at $t = 0.2$.

Following, *a posteriori* results of simulation of the shock propagation using the QSV closure models in Fourier based pseudospectral simulations are gathered in figure B.21. The numerical solution for the pressure, velocity and density fields display excellent agreement with the analytical results showing little influence of spurious oscillations even in relatively coarse simulations. In the spectra plots, a small energy accumulation can be observed but it seems to have little effect on the solution.

Although the high frequency oscillations do not pose a stability concern, they can be undesirable in situations where a quiet flow is preferred. In those situations, the numerically implemented scheme can be made more robust in the sense of decreasing the magnitude of these spurious vibrations by explicitly filtering the spectrum in the near-cutoff region of all the conserved variables, density, momentum and internal energy. This explicit filtering step is not needed for the current simple test case, though.

Appendix C. QSV in Generalized Curvilinear Coordinates

Following Jordan (1999) and Nagarajan et al. (2007), who developed, respectively, the incompressible and compressible LES methodology in generalized curvilinear coordinates, we present the filtered equations and the Quasi-Spectral Viscosity method, when subjected to the necessary grid transformations. Assume the existence of a known, invertible mapping between \mathbf{y} , the physical cartesian reference frame, and \mathbf{x} , the contravariant curvilinear coordinate system,

$$x^i = x^i(y^1, y^2, y^3), \quad (\text{C.1})$$

$$y^i = y^i(x^1, x^2, x^3), \quad (\text{C.2})$$

where x^i and y^i are the i -th coordinate of each respective system of reference. Following, consider the following curvilinear equivalent of Favre filtering,

$$\check{f} = \frac{\overline{J\rho f}}{\overline{J\rho}} \quad (\text{C.3})$$

where J is the Jacobian of the transformation which is the determinant of the Jacobi matrix ($J_{ij} = \partial y^i / \partial x^j$), then the filtered governing equations are

$$\frac{\partial \overline{J\rho}}{\partial t} + \frac{\partial}{\partial x^j} (\overline{J\rho} \check{v}^j) = 0, \quad (\text{C.4})$$

$$\frac{\partial \overline{J\rho} \check{v}^i}{\partial t} + \frac{\partial}{\partial x^j} (\overline{J\rho} \check{v}^i \check{v}^j + \overline{J\rho} g^{ij} - J\check{\sigma}^{ij} + \overline{J\rho} \tau^{ij}) = -\Gamma_{qj}^i (\overline{J\rho} \check{v}^q \check{v}^j + \overline{J\rho} g^{qj} - J\check{\sigma}^{qj} + \overline{J\rho} \tau^{qj}), \quad (\text{C.5})$$

$$\frac{\partial \overline{JE}}{\partial t} + \frac{\partial}{\partial x^j} (\overline{J(E+p)} \check{v}^j + J\check{Q}^j) = \frac{\partial}{\partial x^k} (J\check{\sigma}^{ij} g_{ik} \check{v}^k) - \frac{\partial \overline{J\rho} C_p q^j}{\partial x_j}, \quad (\text{C.6})$$

and the subfilter terms are defined as

$$\tau^{ij} = \widetilde{v^i v^j} - \check{v}^i \check{v}^j, \quad \text{and} \quad q^j = \widetilde{T v^j} - \check{T} \check{v}^j. \quad (\text{C.7})$$

Moreover, the tensors responsible for mapping a curvilinear physical space into an euclidean reference space are the covariant and contravariant metric tensors $g_{ij} = \frac{\partial y^i \partial y^j}{\partial x^k \partial x^k}$, $g^{ij} = \frac{\partial x^k \partial x^k}{\partial y^i \partial y^j}$, respectively, and the Christoffel symbol of the second kind, $\Gamma_{qj}^i = \frac{\partial x^i}{\partial y^q} \frac{\partial^2 y^j}{\partial x^q \partial x^j}$. In the derivation of these equations, the metric tensors and Christoffel symbols are assumed to be varying slowly over the spatial support of the filter kernel, therefore leading to no additional sub filter flux terms.

In the curvilinear frame of reference the total energy, the viscous stress tensor and the heat flux vector are described by slightly modified relations described below:

$$\frac{\overline{J\rho}}{\gamma - 1} = \overline{JE} - \frac{1}{2} \overline{J\rho} g_{ij} \check{v}^i \check{v}^j - \frac{1}{2} \overline{J\rho} g_{ij} \tau^{ij}, \quad (\text{C.8})$$

$$\check{\sigma}^{ij} = \mu \left(g^{jk} \frac{\partial \check{v}^i}{\partial x^k} + g^{ik} \frac{\partial \check{v}^j}{\partial x^k} - \frac{2}{3} g^{ij} \frac{\partial \check{v}^k}{\partial x^k} \right), \quad (\text{C.9})$$

$$\check{Q}^j = -k g^{ij} \frac{\partial \check{T}}{\partial x^i}. \quad (\text{C.10})$$

Ultimately, the proposed closures for τ^{ij} and q^j when applied to generalized curvilinear coordinates are

$$\tau^{ij} = -C_{\tau^{ij}} \frac{1}{2} \left(g^{jk} \frac{\partial \ddot{v}^i}{\partial x^k} + g^{ik} \frac{\partial \ddot{v}^j}{\partial x^k} \right), \quad (\text{C.11})$$

$$q^j = -C_q g^{jk} \frac{\partial \ddot{T}}{\partial x^k}. \quad (\text{C.12})$$

Here, the double dot superscript indicates the filter modulated quantities, defined in curvilinear coordinates as

$$\frac{\partial \ddot{v}^i}{\partial x^k} = \sqrt{2 \|\bar{\Delta} E_{g_{kj} v^k v^j}(k_c)\|} \left[\frac{\partial \check{v}^i}{\partial x^k} * \left(1 - \tilde{G}_{\text{eff}}(\alpha, \beta, w) \right) \right], \quad (\text{C.13})$$

$$\frac{\partial \ddot{T}}{\partial x^k} = \sqrt{2 \|\bar{\Delta} E_{g_{kj} v^k v^j}(k_c)\|} \left[\frac{\partial \check{T}}{\partial x^k} * \left(1 - \tilde{G}_{\text{eff}}(\alpha, \beta, w) \right) \right], \quad (\text{C.14})$$

and the curvilinear 2-norm is defined as

$$\|\bar{\Delta} E_{g_{jk} v^j v^k}(k_c)\| = \sqrt{g_{lm} \bar{\Delta}_l E_{g_{kj} v^k v^j}(k_{c,l}) \bar{\Delta}_m E_{g_{kj} v^k v^j}(k_{c,m})}, \quad (\text{C.15})$$

where $\bar{\Delta}_l$ is the computational grid spacing in each direction, defined by the initial mapping from physical space to a reference space, where the equations are solved.

Acknowledgments

Victor Sousa and Carlo Scalo acknowledge the computational support of the Rosen Center for Advanced Computing (RCAC) at Purdue and of the U.S. Air Force Research Laboratory (AFRL) DoD Supercomputing Resource Center (DSRC), via allocation under the subproject AFOSR43032009. This project was funded by the Air Force Office of Scientific Research (AFOSR) grant FA9550-16-1-0209, the AFOSR YIP (FA9550-18-271-0292), the Office of Naval Research YIP (N000142012662) as well as the ONR Grant No. N00014-21-1-2475. Victor Sousa also acknowledges the support of the Lynn Fellowship administered by the interdisciplinary Computational Science and Engineering (CS&E) graduate program at Purdue University.

References

- Andreassen, Ø., Lie, I., Wasberg, C.E., 1994. The spectral viscosity method applied to simulation of waves in a stratified atmosphere. *Journal of Computational Physics* 110, 257–273.
- Chapelier, J.B., Wasistho, B., Scalo, C., 2018. A coherent vorticity preserving eddy-viscosity correction for large-eddy simulation. *Journal of Computational Physics* 359, 164–182.
- Chen, Y., Scalo, C., 2021. High-speed turbulent channel flows over complex impedance walls. *J. Fluid Mech.* Under Review.

- Chollet, J., Lesieur, M., 1981. Parameterization of small scales of three-dimensional isotropic turbulence utilizing spectral closures. *J. Atmo. Sci.* 38, 2747–2757.
- Cook, A.W., 2007. Artificial Fluid Properties for Large-Eddy Simulation of Compressible Turbulent Mixing. *Physics of fluids* 19, 055103.
- Denet, B., Biamino, L., Lodato, G., Vervisch, L., Clavin, P., 2015. Model equation for the dynamics of wrinkled shockwaves: comparison with dns and experiments. *Combustion Science and Technology* 187, 296–323.
- Ducros, F., Comte, P., Lesieur, M., 1995. Direct and large-eddy simulations of transition of a supersonic boundary layer, in: *Turbulent Shear Flows* 9. Springer, pp. 283–300.
- Ducros, F., Ferrand, V., Nicoud, F., Weber, C., Darracq, D., Gacherieu, C., Poinso, T., 1999. Large-eddy simulation of the shock/turbulence interaction. *Journal of Computational Physics* 152, 517–549.
- Ellzey, J.L., Henneke, M.R., Picone, J.M., Oran, E.S., 1995. The interaction of a shock with a vortex: shock distortion and the production of acoustic waves. *Physics of Fluids* 7, 172–184.
- Fejér, L., 1903. Untersuchungen über fouriersche reihen. *Mathematische Annalen* 58, 51–69.
- Frisch, U., 1995. *Turbulence: the legacy of A. N. Kolmogorov*. Cambridge University Press, Cambridge.
- Germano, M., Piomelli, U., Moin, P., Cabot, W., 1991. A dynamic subgrid-scale eddy viscosity model. *Phys. Fluids A* 3, 1760–1765.
- Gupta, P., Scalo, C., 2018. Spectral energy cascade and decay in nonlinear acoustic waves. *Phys. Rev. E* 98, 033117. URL: <https://link.aps.org/doi/10.1103/PhysRevE.98.033117>, doi:10.1103/PhysRevE.98.033117.
- Huang, P.G., Coleman, G.N., Bradshaw, P., 1995. Compressible turbulent channel flows: DNS results and modelling. *J. Fluid Mech.* 305, 185–218.
- Jordan, S.A., 1999. A large-eddy simulation methodology in generalized curvilinear coordinates. *Journal of Computational Physics* 148, 322–340.
- Karamanos, G., Karniadakis, G.E., 2000. A spectral vanishing viscosity method for large-eddy simulations. *Journal of Computational Physics* 163, 22–50.
- Karniadakis, G., Sherwin, S., 2013. *Spectral/hp element methods for computational fluid dynamics*. Oxford University Press.
- Kawai, S., Lele, S.K., 2008. Localized Artificial Diffusivity Scheme for Discontinuity Capturing on Curvilinear Meshes. *Journal of Computational Physics* 227, 9498–9526.
- Kawai, S., Shankar, S.K., Lele, S.K., 2010. Assessment of localized artificial diffusivity scheme for large-eddy simulation of compressible turbulent flows. *Journal of Computational Physics* 229, 1739–1762.
- Kirby, R.M., Karniadakis, G.E., 2002. Coarse resolution turbulence simulations with spectral vanishing viscosity—large-eddy simulations (svv-les). *J. Fluids Eng.* 124, 886–891.
- Kraichnan, R., 1976. Eddy viscosity in two and three dimensions. *J. Atmo. Sci.* 33, 1521–1536.
- Lele, S.K., 1992. Compact Finite Difference Schemes with Spectral-Like Resolution. *Journal of Computational Physics* 103, 16–42. doi:10.1016/0021-9991(92)90324-R.
- Lilly, D.K., 1992a. A proposed modification of the Germano subgrid-scale closure method. *Physics of Fluids A: Fluid Dynamics* (1989-1993) 4, 633–635.
- Lilly, D.K., 1992b. A proposed modification of the Germano subgrid-scale closure method. *Phys. Fluids A* 4, 633–635.
- Lodato, G., Vervisch, L., Clavin, P., 2016. Direct numerical simulation of shock wavy-wall interaction: analysis of cellular shock structures and flow patterns. *J. Fluid Mech.* 789, 221–258.
- Lodato, G., Vervisch, L., Clavin, P., 2017. Numerical study of smoothly perturbed shocks in the Newtonian limit. *Flow Turb. Comb.* doi:10.1007/s10494-017-9830-1. **in press**.
- Maday, Y., Kaber, S.M.O., Tadmor, E., 1993. Legendre pseudospectral viscosity method for nonlinear conservation laws. *SIAM Journal on Numerical Analysis* 30, 321–342.
- Meneveau, C., Lund, T.S., Cabot, W.H., 1996. A lagrangian dynamic subgrid-scale model of turbulence. *J. Fluid Mech.* 319, 353–385.
- Metais, O., Lesieur, M., 1992. Spectral Large-Eddy Simulation of isotropic and stably stratified turbulence. *J. Fluid Mech.* 239, 157–194.
- Moin, P., Squires, K., Cabot, W., Lee, S., 1991. A dynamic subgrid-scale model for compressible turbulence and scalar transport. *Physics of Fluids A: Fluid Dynamics* (1989-1993) 3, 2746–2757.
- Morkovin, M.V., 1962. Effects of compressibility on turbulent flows. *Mécanique de la Turb.* 367, 380.
- Myers, M.K., 1991. Transport of energy by disturbances in arbitrary steady flows. *Journal of Fluid Mechanics* 226, 383–400.
- Nagarajan, S., Lele, S., Ferziger, J., 2007. Leading-Edge Effects in Bypass Transition. *J. Fluid Mech.* 572, 471–504.
- Nagarajan, S., Lele, S.K., Ferziger, J.H., 2003. A Robust High-Order Compact Method for Large-Eddy Simulation. *Journal of Computational Physics* 191, 392–419.
- Ng, L., Erlebacher, G., 1992. Secondary instabilities in compressible boundary layers. *Phys. Fluids* 4.
- Normand, X., Lesieur, M., 1992. Direct and large-eddy simulations of transition in the compressible boundary layer. *Theoretical and Computational Fluid Dynamics* 3, 231–252.
- Pasquetti, R., 2005. Spectral vanishing viscosity method for les: sensitivity to the svv control parameters. *Journal of Turbulence* 6.
- Pasquetti, R., 2006. Spectral vanishing viscosity method for Large-Eddy simulation of turbulent flows. *J. Sci. Comput.* 27, 365–375.
- Premasuthan, S., Liang, C., Jameson, A., 2014a. Computation of flows with shocks using the spectral difference method with artificial viscosity, i: basic formulation and application. *Computers & Fluids* 98, 111–121.
- Premasuthan, S., Liang, C., Jameson, A., 2014b. Computation of flows with shocks using the spectral difference method with artificial viscosity, ii: Modified formulation with local mesh refinement. *Computers & Fluids* 98, 122–133.
- Rault, A., Chiavassa, G., Donat, R., 2003. Shock-vortex interactions at high mach numbers. *Journal of Scientific Computing* 19, 347–371.
- Shen, J., Tang, T., Wang, L.L., 2011. *Spectral methods: algorithms, analysis and applications*. volume 41. Springer Science & Business Media.
- Shu, C., Osher, S., 1988. Efficient implementation of essentially non-oscillatory shock-capturing schemes. *J. Comput. Phys.* 77, 439–471.
- Sidharth, G., Candler, G.V., 2018. Subgrid-scale effects in compressible variable-density decaying turbulence. *Journal of Fluid Mechanics* 846, 428–459.
- Smagorinsky, J., 1963a. General circulation experiments with the primitive equations. *Monthly Weather Review* 91, 99 – 164.
- Smagorinsky, J., 1963b. General circulation experiments with the primitive equations. *Mon. Weather Rev.* 91, 99–164.
- Sod, G.A., 1978. A survey of several finite difference methods for systems of nonlinear hyperbolic conservation laws. *Journal of computational physics* 27, 1–31.
- Tadmor, E., 1989. Convergence of spectral methods for nonlinear conservation laws. *SIAM Journal on Numerical Analysis* 26, 30–44.

- Tadmor, E., 1990. Shock capturing by the spectral viscosity method. *Computer Methods in Applied Mechanics and Engineering* 80, 197–208.
- Tonicello, N., Lodato, G., Vervisch, L., 2020. Entropy preserving low dissipative shock capturing with wave-characteristic based sensor for high-order methods. *Computers & Fluids* 197, 104357.
- Trettel, A., Larsson, J., 2016. Mean velocity scaling for compressible wall turbulence with heat transfer. *Phys. Fluids* 28, 026102.
- Vandeven, H., 1991. Family of spectral filters for discontinuous problems. *Journal of Scientific Computing* 6, 159–192.
- Vreman, A.W., 2004. An eddy-viscosity subgrid-scale model for turbulent shear flow: Algebraic theory and applications. *Phys. Fluids* 16, 3670.
- Vreman, B., Geurts, B., Kuerten, H., 1995. A priori tests of Large-Eddy Simulation of the compressible plane mixing layer. *Journal of engineering mathematics* 29, 299–327.
- Yoshizawa, A., 1986. Statistical theory for compressible turbulent shear flows, with the application to subgrid modeling. *The Physics of fluids* 29, 2152–2164.